Analytic models of the spectral properties of gravitational waves from neutron star merger remnants

Theodoros Soultanis,[1,2,*] Andreas Bauswein,[3,4] and Nikolaos Stergioulas[5]

[1]*Heidelberg Institute for Theoretical Studies, Schloss-Wolfsbrunnenweg 35, 69118 Heidelberg, Germany*
[2]*Max-Planck-Institut für Astronomie, Königstuhl 17, 69117 Heidelberg, Germany*
[3]*GSI Helmholtzzentrum für Schwerionenforschung, Planckstraße 1, 64291 Darmstadt, Germany*
[4]*Helmholtz Research Academy Hesse for FAIR (HFHF), GSI Helmholtz Center for Heavy Ion Research, Campus 64291 Darmstadt, Germany*
[5]*Department of Physics, Aristotle University of Thessaloniki, 54124 Thessaloniki, Greece*

(Received 16 November 2021; accepted 5 February 2022; published 28 February 2022)

We present a new analytic model describing gravitational-wave emission in the postmerger phase of binary neutron star mergers. The model is described by a number of physical parameters that are related to various oscillation modes, quasilinear combination tones or nonlinear features that appear in the postmerger phase. The time evolution of the main postmerger frequency peak is taken into account and it is described by a two-segment linear expression. The effectiveness of the model, in terms of the fitting factor or, equivalently, the reduction in the detection rate, is evaluated along a sequence of equal-mass simulations of varying mass. We find that all parameters of the analytic model correlate with the total binary mass of the system. For high masses, we identify new spectral features originating from the nonlinear coupling between the quasiradial oscillation and the antipodal tidal deformation, the inclusion of which significantly improves the fitting factors achieved by the model. We can thus model the postmerger gravitational-wave emission with an analytic model that achieves high fitting factors for a wide range of total binary masses. Our model can be used for the detection and parameter estimation of the postmerger phase in upcoming searches with upgraded second-generation detectors, such as aLIGO+ and aVirgo+, with future, third-generation detectors (Einstein Telescope and Cosmic Explorer) or with dedicated, high-frequency detectors.

DOI: 10.1103/PhysRevD.105.043020

I. INTRODUCTION

The two gravitational-wave (GW) events that have been identified as binary neutron star (BNS) mergers, GW170817 [1] and GW190425 [2], offer a glimpse into the many more observations that are anticipated for the next years [3]. Already, the detection of GWs from the inspiral phase of GW170817 produced new constraints on the dimensionless tidal deformability of neutron stars and thus on their equation of state (EOS) [1,4]; see [5,6] for recent reviews. Those detections can be combined with information extracted from the electromagnetic counterpart of GW170817 or other measurements, e.g., [7–17] and references therein. Significant improvement on these EOS constraints is expected by combining a larger number of detections in the near future [18–22]. Although the sensitivity of the Advanced LIGO and Advanced Virgo detectors was not sufficient to detect the postmerger phase in GW170817 [1,4,23], such detections are likely to be achieved in the future, with upgraded [24], with dedicated high-frequency [25–29] or with third-generation [30,31] detectors. Such observations of GWs in the postmerger phase of BNS mergers would offer a tremendous opportunity to probe the high-density EOS; see [13,32–67] and references therein.

In order to detect the postmerger GW phase, robust and efficient data analysis techniques are needed, and currently there are two main approaches. One employs morphology-independent signals [44,52], while the other is based on matched-filtering techniques, which require accurate GW postmerger template banks. We focus our discussion on the latter method. In [40] we introduced a time-domain analytic model, which utilizes a combination of three exponentially decaying sinusoids. The model incorporated the dominant postmerger peak (f_{peak}) and the two most significant secondary frequency components (f_{spiral} and f_{2-0}) that

*theodoros.soultanis@h-its.org

also correlate with the binary's properties. Informed by numerical relativity simulations, frequency-domain models were introduced in [39,50,53,68] and time-domain models were introduced in [35,49,57,69–71]. In [39] a frequency-domain model (which can be inverted to the time domain) was constructed for the amplitude and phase of the spectra, using a principal component analysis. Reference [50] introduced a frequency-domain hierarchical model, which generates amplitude spectra. In [53] a frequency-domain amplitude model, which utilizes Lorentzian functions, in combination with relations connecting binary properties to the postmerger characteristic features was introduced. Reference [49] developed a time-domain analytical model based on the morphology of the postmerger waveforms (employing numerical relativity informed relations), which can be combined with an inspiral waveform. In [57] a time-domain analytic model which uses exponentially damped sinusoids (as in [40]) and includes three frequency components was developed. In this model, for all the frequency components, a constant linear frequency-drift term was introduced.

In order to construct faithful postmerger GW templates, it is important to understand the underlying physical mechanisms, which dictate the different features of the GW spectrum. The latter is complex and even though some of its properties are well studied and understood others are not.

In this work we compare the spectral properties of the postmerger phase along a sequence of equal-mass BNS merger simulations with increasing total mass ($M_{\rm tot}$). We find a smooth transition of spectral features along this sequence as anticipated in [37]. In particular, we study the time evolution of the dominant frequency component ($f_{\rm peak}$) in the GW spectra (see also [57]) and using spectrograms we introduce a time-dependent two-segment piecewise analytic function, which models such a frequency drift.

In addition, we identify a new coupling mechanism between tidal antipodal bulges ($f_{\rm spiral}$; see [37]) and the quasiradial mode (f_0), which results in two frequency peaks in the GW spectra of high-mass models. The inclusion of this new feature significantly improves the fitting factors achieved for systems with binary masses near the threshold mass to prompt collapse.

We develop a time-domain analytic model (based on [40]) for the postmerger GW emission, which incorporates the four frequency components ($f_{\rm peak}$, $f_{\rm spiral}$, and $f_{2\pm0}$) and allows a time-dependent description of the $f_{\rm peak}$ component. We introduce a hierarchical procedure to determine the analytic model's parameters. We evaluate the performance of our analytic model using the noise-weighted fitting factor (FF) and show that this remains higher than ~0.96 along the whole sequence of binary models considered.

Our new analytic model is described by physical parameters only and we find that all parameters correlate with the total binary mass of the system. It can be used for the detection and parameter estimation of the postmerger phase in upcoming searches with upgraded second-generation detectors, such as aLIGO+ and aVirgo+ (see [24]), with future, third-generation (Einstein Telescope [72] and Cosmic Explorer [30]) or with dedicated high-frequency detectors [25–29]. Because the model is based on physical parameters, it elucidates the mechanisms shaping the spectra and how those depend on the binary mass.

This paper is structured as follows: In Sec. II we describe the physical systems we simulate and our numerical setup. In Sec. III we discuss particular features of the GW signal in the postmerger phase for a reference simulation. In Sec. IV we consider a sequence of models with increasing total binary mass $M_{\rm tot}$ and describe how the spectral properties depend on $M_{\rm tot}$. In Sec. V we introduce an analytic time-domain model for the postmerger phase. In Sec. VI we discuss the fits of the analytic model to the simulation data and evaluate its performance using the noise-weighted FF. Section VII addresses the parameters of the analytic model and their dependencies on the total binary mass $M_{\rm tot}$. In Sec. VIII we focus on specific configurations with a total mass $M_{\rm tot}$ close to the threshold mass for prompt collapse $M_{\rm thres}$. In different appendixes, we include more detailed information on various aspects described in the main text.

Unless otherwise noted, we employ a dimensionless system of units for which $c = G = M_\odot = 1$. In Appendix C 4 we summarize the notation and the units for all the parameters of our analytic model.

II. METHODS

We perform three-dimensional fully general relativistic simulations of binary neutron star mergers and discuss the spectral features of the postmerger GW emission. We use the MPA1 [73] EOS. This EOS model is compatible with constraints from GW170817 [74] and with the mass measurement of $2.01 \pm 0.04\ M_\odot$ for pulsar PSR J0348 + 0432 [75]. We simulate a sequence of symmetric binaries (with mass ratio q = 1) varying the total binary mass $M_{\rm tot}$. We consider eight models with $M_{\rm tot} = 2.4$, 2.5, 2.6, 2.7, 2.8, 2.9, 3.0 and 3.1 $M_\odot$. None of the models collapses to a black hole (BH) within the simulation time of up to 25 ms after merging, although the total mass of the most massive binary is close to the threshold binary mass for prompt BH formation $M_{\rm thres}$ [76]. In the following sections we will introduce our results by discussing the model with $M_{\rm tot} = 2.5\ M_\odot$ as a reference simulation and then extend the analysis by including models with other binary masses.

We construct initial data (ID) of circular quasiequilibrium solutions with the LORENE code [77,78]. The initial separation between the centers of the NSs is 40 km, which results in a few revolutions before merging. We assess the impact of residual eccentricity e in the simulations in Appendix A 1. We show that the GW spectral features are hardly affected by eccentricity $e < 0.01$.

For the evolution we employ the Einstein Toolkit code [79]. The hydrodynamics are solved by the GRHydro module [80,81] adopting the Valencia formulation [82,83]. We use the HLLE Riemann solver [84] and weighted essentially non-oscillatory (WENO) reconstruction [85,86]. The spacetime evolution is carried out in the Z4c formulation [87,88] as implemented in the CTGamma module [89,90]. The computational domain consists of seven refinement levels where the inner one has the finest resolution ($dx = 277$ m) while the grid spacing is doubled at each successive level. The box size corresponds to $x_{\rm max} = 2126.276$ km. In Appendix A 2 we describe an additional simulation with better resolution ($dx = 185$ m) and find an only weak influence on the GW spectral features. In the following sections we will refer to this calculation as HR simulation and will indicate the respective results in various figures.

To reduce the computational costs we impose reflection symmetry with respect to the orbital plane and pi symmetry with respect to the axis normal to this plane. We have also performed additional simulations without the pi symmetry and find that the impact on the spectral properties is negligible (see Appendix A 3).

The EOS is implemented as a seven-segment piecewise polytrope [91] and is supplemented with an ideal-gas pressure component to approximate thermal effects, where we set $\Gamma_{\rm th} = 1.75$ (see e.g., [92] justifying this value as a reasonable choice to model the postmerger GW emission).

We extract GWs employing the Ψ_4 formalism. The Weyl scalar Ψ_4 is decomposed in spin-weighted spherical harmonics at a finite coordinate radius R, where the radially averaged component is denoted by $\Psi_4^{l,m}(t, R)$. We focus on the dominant mode $(l, m) = (2, 2)$. We use an extraction coordinate radius of $R \simeq 443$ km (but we tested also a larger extraction coordinate radius of $R \simeq 1033$ km and find that the GW spectra are essentially unaffected). Computing the strain requires a double integration of $\Psi_4^{l,m}(t, R)$ with respect to coordinate time t, which leads to nonlinear drifts in the strain. To avoid this problem, we perform the integration in the frequency domain using a fixed frequency integration scheme [93].

We define the merging time $t_{\rm merge}$ as the time at which $|h(t)| = \sqrt{h_+^2(t) + h_\times^2(t)}$ reaches the maximum. We perform a time shift ($t \to t - t_{\rm merge}$) so that $t = 0$ corresponds to the merging time. We split the GW signals into two phases accordingly: (a) the inspiral phase ($t < 0$) and (b) the postmerger phase ($t \geq 0$). All figures associated with GW quantities (such as GW spectrograms) use the aforementioned convention meaning that $t = 0$ corresponds to the merging time obtained from $\max|h(t)|$. Figures and measures associated with the lapse function (such as spectrograms of the minimum lapse function $\alpha_{\rm min}$) define the merging time using the maximum of strain obtained from the quadrupole formula $|h^{\rm QF}(t)|$. We note that (prior to our time shifting) the two times of the $\max|h(t)|$ and $\max|h^{\rm QF}(t)|$ should differ by approximately $\Delta t \simeq \frac{1}{c} R \simeq 1.5$ ms, which thus can be removed as appropriate.

III. SPECTRAL ANALYSIS OF THE POSTMERGER GW EMISSION FOR A REFERENCE SIMULATION

First, we consider the model with $M_{\rm tot} = 2.5\ M_\odot$ as a *reference simulation* and discuss the different features of the postmerger GW signal. We describe how we extract those features from the simulation data and how we include them in an analytic model for the postmerger phase. Apart from considering the features present in the GW spectrum, we also also extract the time evolution of certain features by computing spectrograms. Throughout this work and for the sake of simplicity, we will often use a frequency, for example, $f_{\rm peak}$, to refer to a specific peak in the spectrum or mode of the GW signal.

A. Evolution of $f_{\rm peak}$ and analytic fit

The strongest feature in the postmerger gravitational-wave signal is attributed to the fundamental quadrupolar oscillation mode (see [35,38–40,48,94–106]). Its frequency, usually denoted as $f_{\rm peak}$ (or f_2), dominantly depends on the EOS and the total binary mass. This is expected since the high-density regime of the EOS dictates the size of the remnant. As the remnant undergoes further evolution, $f_{\rm peak}$ shifts to higher or lower frequencies. The interplay of cooling and angular momentum redistribution as well as losses leads to a change of the stellar structure and thus to a change in the dominant oscillation frequency.

In order to understand the frequency evolution of particular components in the GW signal, we compute spectrograms that employ a wavelet-based scheme [107]. The spectrogram in Fig. 1 displays the time evolution of the dominant component $f_{\rm peak}$ of our reference simulation. In the first few milliseconds, $f_{\rm peak}$ undergoes a rapid evolution, and the signal can be split in two phases: (a) for $t \lesssim 6$ ms, $f_{\rm peak}$ follows a decreasing trend approximately from about 2.8 to 2.5 kHz; (b) for $t \gtrsim 6$ ms, $f_{\rm peak}$ is approximately constant with $f_{\rm peak} = 2.5$ kHz. We quantify the drift by extracting the evolution of $f_{\rm peak}(t)$ from the spectrogram (black curve) as the frequency which corresponds to the maximum wavelet coefficient at time t. We model $f_{\rm peak}(t)$ with a simple two-segment piecewise *analytic fit* with respect to the time coordinate t. The first segment describes the initial drift as a linear function in the frequency-time plane, while the second segment assumes a constant $f_{\rm peak}$, imposing continuity as

$$f_{\rm peak}^{\rm analytic}(t) = \begin{cases} \zeta_{\rm drift} \cdot t + f_{\rm peak,0} & \text{for } t \leq t_*, \\ f_{\rm peak}(t_*) & \text{for } t > t_*. \end{cases} \quad (1)$$

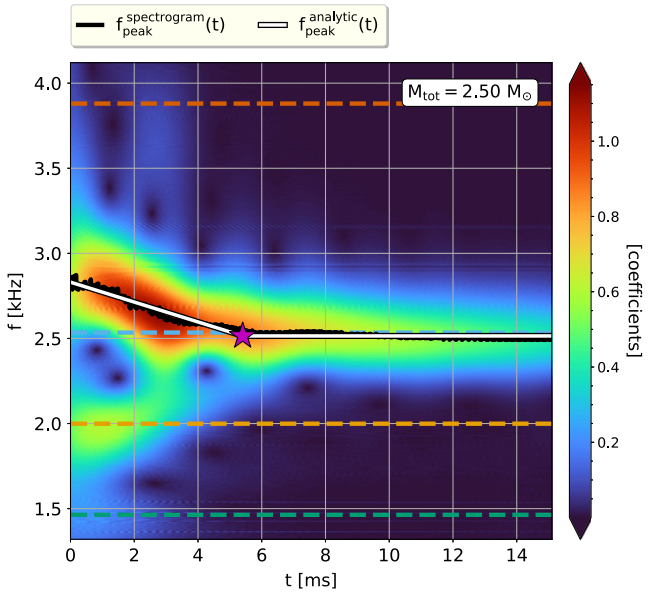

FIG. 1. Spectrogram of strain $h_+(t)$ for the reference simulation. The black curve illustrates $f_{\rm peak}(t)$ determined by the maximum wavelet coefficient at given time t. The white curve shows the two-segment piecewise analytic fit $f_{\rm peak}^{\rm analytic(t)}$ of Eq. (1). The purple star indicates $t = t_*$, after which the frequency remains constant. The cyan, yellow, green, and orange dashed horizontal lines indicate $f_{\rm peak}$, $f_{\rm spiral}$, f_{2-0}, and f_{2+0}, respectively, as extracted from the spectrum shown in Fig. 2.

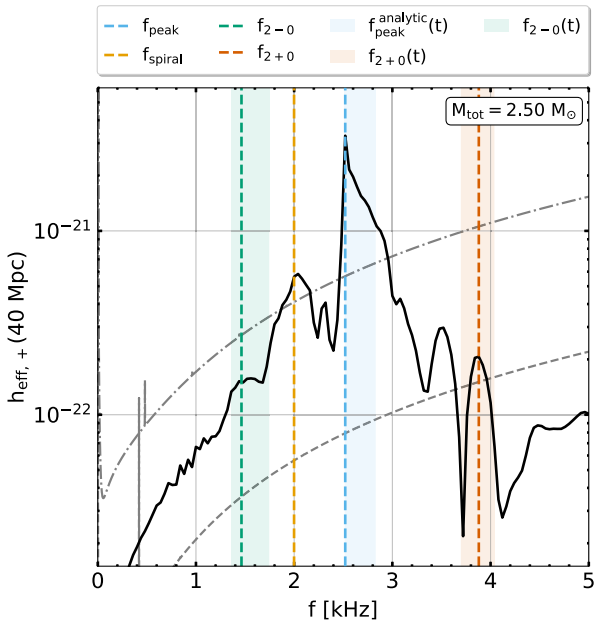

FIG. 2. Effective GW spectrum $h_{\rm eff,+}(f)$ for the postmerger phase of the reference simulation. Colored dashed vertical lines indicate the frequency peaks $f_{\rm peak}$, $f_{\rm spiral}$, f_{2-0}, and f_{2+0}. Shaded areas correspond to the frequency range of $f_{\rm peak}$, f_{2-0}, and f_{2+0} (see text for details). The dash-dotted curves denote the design sensitivity Advanced LIGO [108] and of the Einstein Telescope [109], respectively.

The analytic fit is shown as two white line segments in Fig. 1 and is in good agreement with the numerically extracted $f_{\rm peak}(t)$. Notice that Fig. 1 shows a particular example, with an initial negative drift. In the parameter space of different EOSs and masses, the initial drift can be positive or nearly zero and there are also cases which can be better described by a constant drift up to the delayed collapse to a black hole (these cases can also be covered by the above analytic description).

Throughout this work, $f_{\rm peak}$, i.e., without explicit time argument, denotes the frequency corresponding to the maximum amplitude of $h_{\rm eff,+}(f) = f \cdot \tilde{h}_+(f)$, where $\tilde{h}_+(f)$ is the Fourier transform of $h_+(t)$ (in agreement with the definition currently used in the literature) and $f_{\rm peak}(t)$ refers to dominant frequency as a dynamical quantity, which is extracted from the spectrogram. Below we use this notation for other components of the signal as well. As shown in Fig. 2, the frequency peak may not be symmetric, but it can have a broader, one-sided distribution toward higher frequencies. This feature is explained by an evolving $f_{\rm peak}(t)$ which covers the corresponding frequency range; see also Sec. VI A. The cyan-shaded area in Fig. 2 shows the frequency range as covered by our analytic piecewise function $f_{\rm peak}^{\rm analytic}(t)$, in agreement with the one-sided peak of the dominant mode.

From the spectrograms we also extract a mean value of $f_{\rm peak}(t)$ averaged over the initial interval from 0 to t_*. This mean value $\langle f_{\rm peak}^{t\in[0,t*]}(t)\rangle$ does not necessarily coincide very well with the maximum in the power spectrum, but it provides a measure for $f_{\rm peak}(t)$ at early times.

B. Secondary GW peaks $f_{2\pm0}$ and $f_{\rm spiral}$

As it is apparent from the spectrogram (see Fig. 1) and the spectrum (see Fig. 2) the postmerger GW signal contains several additional secondary features apart from the dominant oscillation mode. Two of those subdominant features originate from a nonlinear coupling between the quadrupolar mode and the quasiradial oscillation mode f_0. This coupling is expected to produce side peaks (combination tones) of the dominant peak at frequencies $f_{2\pm0} \approx f_{\rm peak} \pm f_0$. Inspecting the GW spectrum in Fig. 2, we indeed identify secondary peaks at approximately $f_{\rm peak} \pm f_0$, where we estimate f_0 from a Fourier transform of the evolution of the minimum lapse function, since f_0 (being a quasiradial oscillation) does not occur prominently in the GW spectrum.

In our analysis we extract and define $f_{2\pm0}$ as the corresponding local maxima in the effective power spectrum $h_{\rm eff,+}(f)$ (employing the full signal including the inspiral), where we note that the relation $f_{2\pm0} = f_{\rm peak} \pm f_0$ holds only approximately. This slight inequality is due to

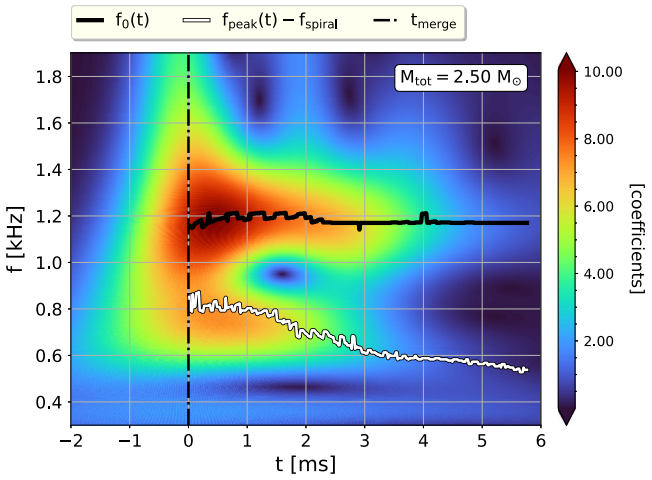

FIG. 3. Spectrogram of minimum lapse function $\alpha_{\rm min}(t)$ for the reference simulation. The black curve shows $f_0(t)$, as determined by the maximum wavelet coefficient at time t. The white line shows $f_{\rm peak}(t) - f_{\rm spiral}$. The vertical dash-dotted line indicates the merging time $t_{\rm merge}$.

the fact that the frequencies of the $f_{2\pm0}$ peaks are determined during the early, very dynamical evolution of the remnant, when the radial oscillation is still strongly excited. In this very early postmerger period, the main frequency peaks, in particular, $f_{\rm peak}(t)$, can evolve rapidly.

In this regard, we further investigate the time evolution of $f_0(t)$. We extract the quasiradial oscillation from the time evolution of minimum lapse function $\alpha_{\rm min}$ (or from the maximum rest mass density ρ_c). Figure 3 shows the spectrogram of the minimum lapse function $\alpha_{\rm min}(t)$. For our reference simulation, the frequency change of $f_0(t)$ is small and comparable to the noise associated to the spectrogram scheme [for high-mass configurations the frequency drift of $f_0(t)$ is slightly more pronounced; see Sec. IV]. The roughly constant frequency $f_0(t)$ is in good agreement with the maximum in the power spectrum of $\alpha_{\rm min}$, as shown in Fig. 7.

Finally, we consider the time evolution of both $f_{\rm peak}(t)$ and $f_0(t)$ to obtain $f_{2\pm0}(t) = f_{\rm peak}(t) \pm f_0(t)$. In Fig. 2 the green and orange bands indicate the ranges in which $f_{2\pm0}(t)$ varies and which coincide well with the secondary peaks.

As already noted, the exact values of the $f_{2\pm0}$ peaks deviate by some percent from $f_{\rm peak} \pm f_0$, i.e., the frequencies extracted from the full signal, which is a consequence of the initial evolution of the main peak frequency $f_{\rm peak}(t)$. Employing the average $\langle f_{\rm peak}^{t\in[0,t_*]}(t)\rangle$ being more representative for the initial phase, we find an excellent agreement between $f_{2\pm0}$ and $\langle f_{\rm peak}^{t\in[0,t_*]}(t)\rangle \pm f_0$. This is understandable, because f_0 decays in comparison to $f_{\rm peak}$ relatively fast, which is why one may expect that the coupling between both modes is shaped by the early $f_{\rm peak}(t)$.

Another secondary peak, $f_{\rm spiral}$, originates from the orbital motion of tidal antipodal bulges [37] formed at the merging phase. Their angular frequency is lower than the one of the inner remnant, and this component is present only for a few cycles [37]. We consider $f_{\rm spiral}$ to be constant in time and define $f_{\rm spiral}$ as the maximum of the corresponding peak at the GW spectrum. There may be a slight evolution of the frequency of $f_{\rm spiral}$ as the central remnant evolves in time and thus affects the motion of the bulges generating $f_{\rm spiral}$. At approximately $t = 3$ ms (and $f = 2.20$ kHz) in Fig. 1 a frequency increase of $f_{\rm spiral}$ is observed. This drift can be seen more clearly in spectrograms with different wavelet parameters, which enhance the frequency resolution. However, since the amplitude of the $f_{\rm spiral}$ feature decays rapidly, we expect the impact of the frequency evolution to be small. In our reference simulation $f_{\rm spiral}$ is the strongest secondary frequency peak and therefore an additional low-frequency modulation $f_{\rm peak}(t) - f_{\rm spiral}$ is expected to affect the remnant's compactness and thus the evolution of $\alpha_{\rm min}(t)$ [37]. This modulation is indeed seen in our reference simulation's spectrogram of $\alpha_{\rm min}(t)$ (see Fig. 3), where we overplot the extracted $f_{\rm peak}(t) - f_{\rm spiral}$.

C. $f_{\rm spiral-0}$ coupling

In this subsection we present our findings about a new mechanism which explains additional frequency peaks in the GW power spectrum, specifically, a coupling between $f_{\rm spiral}$ and the quasiradial oscillation mode f_0. To illustrate this, we discuss the model with a total binary mass $M_{\rm tot} = 3.0\ M_\odot$ (see Fig. 4) where this feature is more pronounced. In this configuration, the total binary mass $M_{\rm tot}$ is close to $M_{\rm thres}$ and therefore the quasiradial mode is strongly excited [37]. In this model, an $f_{\rm spiral}$ component is clearly present. We thus conjecture that the strong radial oscillation affects the motion of the bulges and leads to a coupling between f_0 and $f_{\rm spiral}$. And indeed, we find additional frequency peaks at approximately $f_{\rm spiral\pm0} = f_{\rm spiral} \pm f_0$.

Figure 4 illustrates the postmerger power spectrum for this simulation. As before, we extract the quasiradial oscillation frequency f_0 from the maximum in the Fourier transform $\tilde{\alpha}_{\rm min}(f)$ of the minimum lapse function (see Fig. 7) and obtain the estimates for $f_{\rm spiral\pm0}$ using $f_{\rm spiral}$ from the GW spectrum. In Fig. 4 the estimates $f_{\rm spiral\pm0}$ match very well with additional frequency peaks in the power spectrum. The frequency $f_{\rm spiral} - f_0$ is in better agreement with the corresponding frequency peak while the high-frequency $f_{\rm spiral} + f_0$ deviates by roughly 200 Hz. To further assess our conjecture, we extract the time evolution of $f_0(t)$ from the spectrogram of $\alpha_{\rm min}(t)$ (see Fig. 3) to estimate the frequency ranges of $f_{\rm spiral\pm0}$. These ranges are in good agreement with the additional peaks in the GW spectrum. In particular, the frequency peak in the

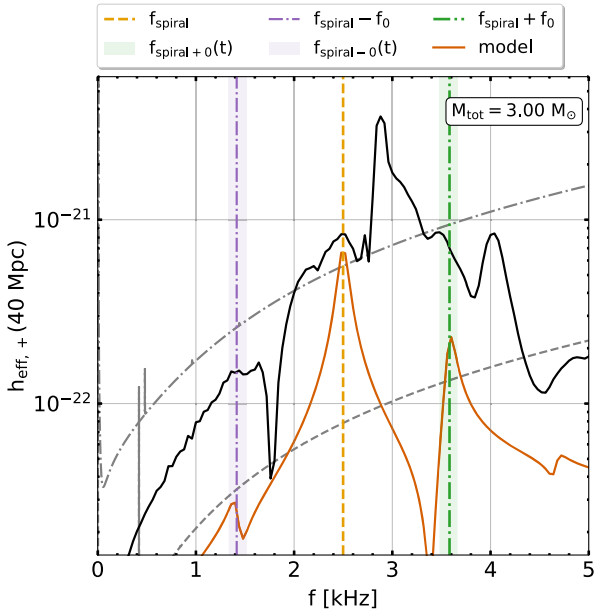

FIG. 4. Effective GW spectrum $h_{\mathrm{eff},+}(f)$ for the $M_{\mathrm{tot}} = 3.0\ M_\odot$ model at postmerger phase. Colored vertical lines indicate f_{spiral}, $f_{\mathrm{spiral}-0}$, and $f_{\mathrm{spiral}+0}$. Shaded areas correspond to their frequency range visualized by the same colors respectively. Orange curve shows the effective GW spectrum of a simple analytic toy model discussed in Sec. III C.

vicinity of $f_{\mathrm{spiral}} + f_0$ lies in the corresponding range. Since in reality f_{spiral} is not exactly constant, a 200 Hz deviation may be understandable. We emphasize that our finding is not unique for this EOS model but it is a general feature in merger simulations. We observe it in additional GW spectra of additional simulations carried out with an smooth particle hydrodynamics (SPH) code [110,111] with varying EOSs and total mass M_{tot}.

We further corroborate our finding by considering a simple analytic toy model: We adopt two point particles with individual masses $m_1 = m_2 = 0.2\ M_\odot$ on an orbit with an orbital frequency $f_{\mathrm{orb}} = \frac{f_{\mathrm{spiral}}}{2}$ at a radius $R = 9$ km. We add a radial oscillation with frequency f_0 superimposed on the circular orbit with amplitude $A = 1.0$ km. These values may be representative of typical simulations. To mimic the fact that the bulges disappear after a few milliseconds we assume an exponential decay of the point-particle masses with a timescale $\tau_{\mathrm{m}} = 5.0$ ms. Finally, we compute the corresponding GW radiation employing the quadrupole formula and derive the Fourier transform, which we overplot in Fig. 4. Interestingly, this simple model produces a strong peak at f_{spiral} (as expected) and two secondary peaks which coincide with $f_{\mathrm{spiral}} \pm f_0$. Note the same pattern of the relative amplitudes of $f_{\mathrm{spiral}} \pm f_0$ in the simulation and the analytic toy model; $f_{\mathrm{spiral}} + f_0$ is significantly enhanced.

Finally, we note that the coupling to the quasiradial mode f_0 may result in frequency peaks at approximately $f_{\mathrm{peak}}(t) \pm 2 \cdot f_0$ and $f_{\mathrm{spiral}} \pm 2 \cdot f_0$. These components are expected to be weak; however for high total mass models, where the f_0 mode is strongly excited, they may become more significant. Our simple analytic toy model generates a peak (in its spectrum) at approximately $f = 4.7$ kHz which coincides with $f_{\mathrm{spiral}} + 2 \cdot f_0$. A weak bump in the GW spectrum can be seen in the vicinity of $f_{\mathrm{spiral}} + 2 \cdot f_0$. In Sec. VIII we identify more features in the GW spectrum which can be associated to such couplings.

IV. SEQUENCE OF MERGER SIMULATIONS WITH DIFFERENT TOTAL BINARY MASS

In this section we discuss a sequence of merger simulations with different total binary masses, in the range of 2.4–3.0 $M_\odot$, with a step size of 0.1 $M_\odot$ (which includes the reference simulation) and we describe how the different components of the postmerger GW signal depend on M_{tot}. We find a smooth transition between the GW spectra along the sequence and observe that the presence and strength of the different spectral features continuously change with total binary mass M_{tot} as it approaches the binary mass for prompt BH formation M_{thres}. Figure 5 shows the effective GW spectra $h_{\mathrm{eff},+}(f)$ for different M_{tot}, where the f_{peak}, f_{spiral}, $f_{2\pm0}$ and $f_{\mathrm{spiral}-0}$ peaks are indicated. As in the previous sections, we assume a distance of 40 Mpc and overplot the sensitivity curves of Advanced LIGO and the Einstein Telescope for reference.

A. Secondary GW peaks

In Fig. 5, the main as well as the secondary peaks show a clear dependence on the total binary mass. The morphology of the GW spectra broadly follows the classification of the postmerger GW signals as in [37], which is based on the presence and relative strength of the secondary peaks. In *low-mass* configurations ($M_{\mathrm{tot}} \leq 2.6\ M_\odot$) f_{2-0} and f_{spiral} are well separated and f_{2-0} is relatively weak because the quasiradial mode is not strongly excited. For *high-mass* configurations ($M_{\mathrm{tot}} \geq 2.8\ M_\odot$), f_{2-0} becomes more pronounced and there is a noticeable overlap between f_{2-0} and f_{spiral}. The absolute height of the f_{spiral} peak is roughly constant in all models, whereas the f_{2-0} feature becomes stronger with higher total binary mass [by nearly one order of magnitude in $h_{\mathrm{eff},+}(f)$].

The secondary frequency peak f_{2+0} is, in most models, observationally less interesting because of its lower amplitude, when compared to the other secondary peaks, and because of the lower sensitivity of current detectors at higher frequencies. However, for the two models with the highest mass within our sequence, the amplitude of f_{2+0} becomes comparable to the amplitude of the other secondary peaks and so it becomes observationally relevant. Interestingly, the frequency f_{2+0} only mildly depends on M_{tot} and ranges between 3.8 and 4.0 kHz for the whole

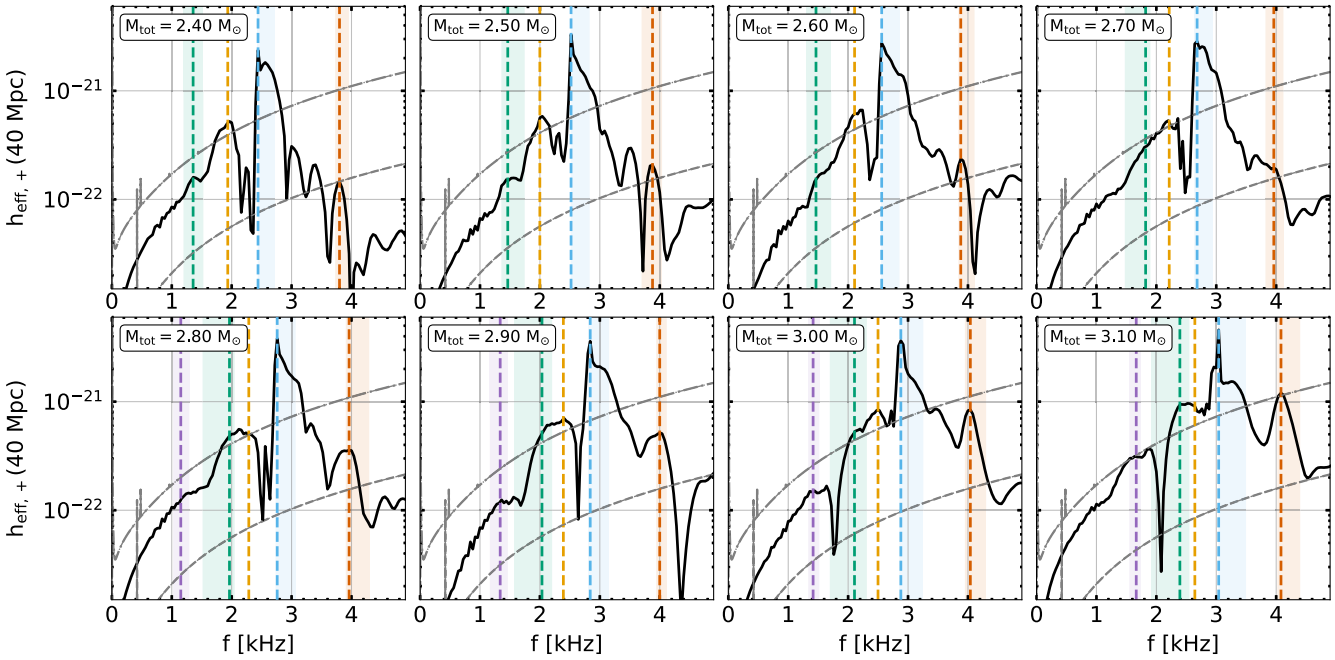

FIG. 5. Effective GW spectra $h_{\mathrm{eff},+}(f)$ for the mass sequence. Purple dashed lines indicate $f_{\mathrm{spiral}-0}$. Purple shaded areas correspond to frequency ranges. The other colors follow the notation of Fig. 2.

mass sequence. The latter is due to f_{peak} being an increasing function of M_{tot} while f_0 decreases.

Only the high-mass configurations (and especially the ones with total mass $M_{\mathrm{tot}} \geq 2.9\ M_\odot$) exhibit a significant frequency peak $f_{\mathrm{spiral}-0}$ (see purple dashed line in Fig. 5). Since f_{spiral} grows with M_{tot} while f_0 slightly decreases, the frequency $f_{\mathrm{spiral}-0}$ increases as the total binary mass approaches the threshold binary mass for prompt collapse M_{thres}. The strength of the $f_{\mathrm{spiral}-0}$ peak increases with the total binary mass M_{tot}. Its absolute height is always smaller than that of the other secondary features, but relative to the projected detector sensitivity curves, the signal to noise ratio of the $f_{\mathrm{spiral}-0}$ coupling is roughly comparable to that of f_{2+0}. The $f_{\mathrm{spiral}-0}$ feature is thus important for configurations with binary masses close to M_{thres}, where the quasiradial mode is strongly excited, which enhances both $f_{\mathrm{spiral}-0}$ and $f_{2\pm0}$ (see lower right panel in Fig. 5).

B. Minimum of the lapse function

As in [37], we investigate the time evolution of the minimum lapse function α_{min}. Figure 6 shows that the behavior of $\alpha_{\mathrm{min}}(t)$ for all models along the sequence is consistent with the respective GW spectra and shows a clear dependence on M_{tot}. As already noted for the models in [37], the quasiradial mode is stronger excited with increasing total binary mass M_{tot}, which explains the enhancement of those GW features that involve a coupling to this particular oscillation mode. For lower-mass and intermediate-mass models the quasiradial mode is only weakly excited. Instead, $\alpha_{\mathrm{min}}(t)$ features an additional oscillation with lower frequency $f_{\mathrm{peak}}(t) - f_{\mathrm{spiral}}$, which dominates during the early phase of the remnant evolution. This modulation is explained by the impact of the massive orbiting bulges generating f_{spiral} on the remnant compactness (see [37] for details).

In general, the behavior in Fig. 6 can be understood from the merger dynamics and remnant properties. High-mass models lead to a collision with a higher impact velocity and thus the quasiradial oscillation is strongly excited.

The aforementioned features in the minimum lapse function can be identified in the power spectra of the Fourier transform $\tilde{\alpha}_{\mathrm{min}}(f)$, as shown in Fig. 7 (see also [45]).

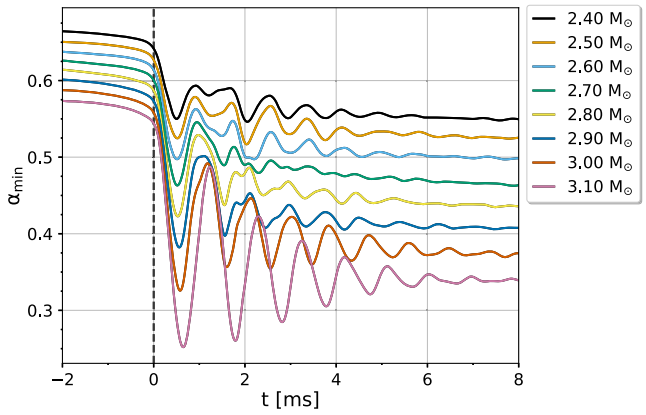

FIG. 6. Time evolution for minimum lapse function $\alpha_{\mathrm{min}}(t)$ normalized to merging time t_{merge} along the sequence of models with varying M_{tot}. Black vertical dashed line shows the merging time t_{merge}.

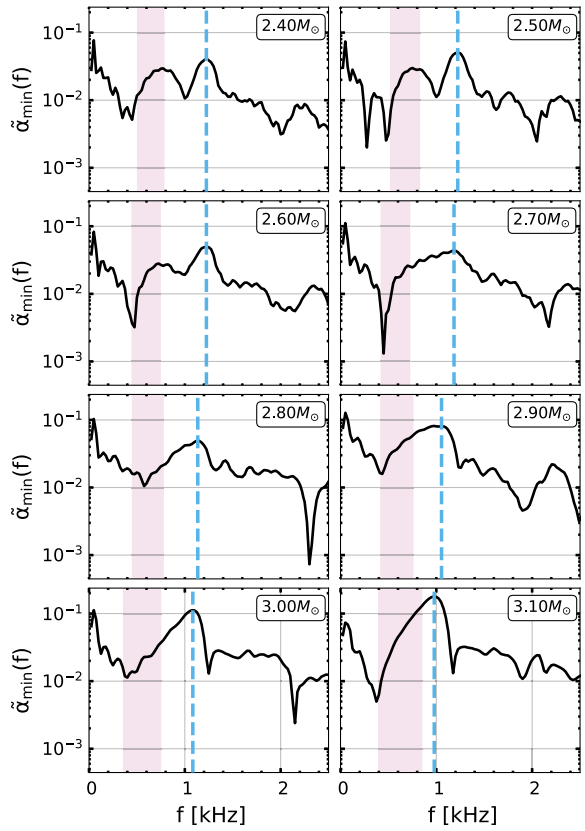

FIG. 7. Fourier transform of the minimum lapse function $\alpha_{\rm min}$ along the sequence models with varying $M_{\rm tot}$. The vertical dashed line indicates the quasiradial frequency f_0. The red band indicates the frequency range of $f_{\rm peak}(t) - f_{\rm spiral}$.

We compute $\tilde{\alpha}_{\rm min}(f)$ using an appropriate window function to select only the postmerger phase.

A common feature in all models is the pronounced quasiradial oscillation frequency peak f_0 in the vicinity of 1 kHz. In low-mass configurations we observe an additional peak at lower frequencies, which corresponds to the $f_{\rm peak}(t) - f_{\rm spiral}$ modulation with a strength comparable to that of the quasiradial mode. Even in cases where the $f_{\rm peak}(t) - f_{\rm spiral}$ modulation appears dominant in the initial phase in the time domain (see Fig. 6), the f_0 peak in the postmerger spectrum is stronger, because the quasiradial mode oscillates longer.

High-mass configurations show a very dominant frequency peak f_0. The strength of the peak increases with $M_{\rm tot}$, and the peak becomes broader and one-sided. This suggests that the quasiradial frequency undergoes an evolution, which can be verified by spectrograms of $\alpha_{\rm min}$ (see Appendix B). Intermediate-mass models show that the $f_{\rm peak}(t) - f_{\rm spiral}$ peak overlaps and merges with the f_0 peak, as $M_{\rm tot}$ increases. We remark in particular for models with higher masses that $f_{\rm peak}(t)$ initially evolves rapidly toward lower values and is initially higher than the $f_{\rm peak}$ identified in the GW spectrum (see Appendix B). Hence, at early times, when the low-frequency modulation is present, the difference $f_{\rm peak}(t) - f_{\rm spiral}$ is in fact larger than one would infer from an inspection of the GW spectrum alone and in high-mass models it is roughly consistent with the left side of the main peaks in Fig. 7. In Fig. 7 we show the estimates for the frequency ranges for $f_{\rm peak}(t) - f_{\rm spiral}$ (red band).

C. Evolution of frequencies

As in the case of the reference simulation of Sec. III, all postmerger GW spectra along the sequence of models (see Fig. 5) exhibit an asymmetric (one-sided) peak, due to the time evolution of $f_{\rm peak}(t)$. The exact morphology somewhat varies as the total mass increases. We quantify the respective drifts in $f_{\rm peak}(t)$ and fit a two-segment piecewise linear or constant function $f_{\rm peak}^{\rm analytic}(t)$, as shown for the reference simulation in Sec. III A [see Appendix B for the spectrograms used in extracting the time evolution of $f_{\rm peak}(t)$ and Sec. VII A for empirical fits as a function of $M_{\rm tot}$ of the parameters of $f_{\rm peak}^{\rm analytic}(t)$ along our sequence of models]. For each model along the sequence, the analytic fit $f_{\rm peak}^{\rm analytic}(t)$ provides a frequency range, which we indicate by cyan bands in Fig. 5 and which coincides well with the full structure of the main peak in the different spectra.

In a similar way, we proceed with the nonlinear couplings between the quadrupolar and the quasiradial mode to estimate a frequency range of these secondary peaks. We extract $f_0(t)$ from the spectrogram of the minimum lapse function $\alpha_{\rm min}(t)$ and employ $f_{\rm peak}^{\rm analytic}(t)$ to obtain a time evolution of $f_{2\pm0}(t) = f_{\rm peak}^{\rm analytic}(t) \pm f_0(t)$. Considering the evolution of $f_{2\pm0}(t)$ during the first milliseconds provides frequency ranges, which we overplot in Fig. 5 (green and orange bands) and which very well agree with the $f_{2\pm0}$ peaks.

We also estimate the frequency range of the coupling between the $f_{\rm spiral}$ and the quasiradial mode (for high-mass configurations) using the time-dependent $f_{\rm spiral-0}(t) = f_{\rm spiral} - f_0(t)$. We overplot them (see Fig. 5) and find a very good agreement with the $f_{\rm spiral-0}$ peak.

As in the case of the reference simulation, it is seen that also for other binary masses the main frequency $f_{\rm peak}$ in Fig. 5 does not exactly occur in the middle between f_{2-0} and f_{2+0} as one would expect for $f_{2\pm0}$. Instead, since the combination tones are rapidly evolving features, we find that $\langle f_{\rm peak}^{t\in[0,t_*]} \rangle$ [which is higher than $f_{\rm peak}$ in all models and more representative for $f_{\rm peak}(t)$ at early times] does indeed agree very well with $\frac{1}{2}(f_{2-0} + f_{2+0})$; i.e., it lies as expected in the middle between the two secondary peaks.

V. ANALYTIC AND SEMIANALYTIC POSTMERGER MODELS

In this section we use our analysis of the postmerger GW signal to build analytic waveform models for the postmerger phase. We construct an *accurate analytic model* of the postmerger GW signal, as an extension of [40], which included fixed $f_{\rm peak}$, $f_{\rm spiral}$ and f_{2-0} frequencies with exponential damping, and of [57], which introduced a linear time dependence of $f_{\rm peak}(t)$ with a constant slope throughout the time evolution. In comparison to these previous works, we also include the higher-frequency combination tone f_{2+0} and use the two-segment piecewise linear model of Eq. (1) to describe the time evolution of $f_{\rm peak}(t)$. The model can easily be extended to include additional features, such as $f_{\rm spiral-0}$ for high masses and we do so in Sec. VIII.

In addition to the fully analytic model, we also consider a *semianalytic model* which incorporates directly a numerical representation of $f_{\rm peak}(t)$ extracted from the spectrograms. This is extended in Sec. VIII to also include time-dependent secondary components $f_{2\pm0}(t)$.

Since the models include a relatively large number of parameters, we employ several successive steps in order to determine the model's parameters. We describe these steps in the following subsections.

A. Analytic model

The analytic model employs exponentially decaying sinusoids and except for the main frequency $f_{\rm peak}(t)$ we assume all other frequencies of the model to be constant in time. The model reads

$$\begin{aligned} h_+(t) = {} & A_{\rm peak}\, e^{(-t/\tau_{\rm peak})} \cdot \sin(\phi_{\rm peak}(t)) \\ & + A_{\rm spiral}\, e^{(-t/\tau_{\rm spiral})} \cdot \sin(2\pi f_{\rm spiral} \cdot t + \phi_{\rm spiral}) \\ & + A_{2-0}\, e^{(-t/\tau_{2-0})} \cdot \sin(2\pi f_{2-0} \cdot t + \phi_{2-0}) \\ & + A_{2+0}\, e^{(-t/\tau_{2+0})} \cdot \sin(2\pi f_{2+0} \cdot t + \phi_{2+0}), \end{aligned} \tag{2}$$

where the $f_{\rm peak}$ component's phase $\phi_{\rm peak}(t)$ is

$$\phi_{\rm peak}(t) = \begin{cases} 2\pi\,(f_{\rm peak,0} + \frac{\zeta_{\rm drift}}{2}t)t + \phi_{\rm peak}, & \text{for } t \le t_*, \\ 2\pi\, f_{\rm peak}(t_*)(t - t_*) + \phi_{\rm peak}(t_*), & \text{for } t > t_*. \end{cases} \tag{3}$$

Using the above expression, the phase $\phi_{\rm peak}(t)$ is continuous and the frequency $f_{\rm peak}(t) = \frac{1}{2\pi}\frac{d\phi_{\rm peak}(t)}{dt}$ features a time dependence as in Eq. (1).

We employ several steps to determine the analytic model's parameters and the model contains several frequency components, which is why it is not straightforward to find the optimal values describing the data. We find that by introducing a *normalization factor* $\mathcal{N}$ we obtain better fits. We thus define

$$h_+^{\rm Fit}(t) = \mathcal{N} \cdot h_+(t), \tag{4}$$

with $h_+(t)$ given as in Eq. (2). We note that when simpler (underperforming) analytic models are employed (consisting of only one or two frequency components) the normalization factor $\mathcal{N}$ is dropped. We stress that the normalization factor is only introduced as part of our procedure for determining the best fit—with other fitting procedures it may not be required.

Lastly, in order to improve the fits for this particular mass sequence and EOS we introduce a *phenomenological modification* to the analytic model in the description of the $f_{\rm peak}(t)$ component. Our quasilinear model of Eq. (2) does not accurately capture the very early evolution presumably because of the nonlinearities that are present immediately after merger. We observe a mild delay in the starting times of the exponentially decaying sinusoids between the $f_{\rm peak}$ component and the secondary components $f_{\rm spiral}$ and $f_{2\pm0}$ during the first $\approx$1.0 ms (see the spectograms in Appendix B). This delay is more pronounced in high-mass configurations. We mimic this delay by multiplying the first line of Eq. (2), which corresponds to the $f_{\rm peak}$ component, by a Tukey window function, denoted here by $\mathcal{W}(t; s)$, where s is the roll-off parameter. We use a roll-off parameter $s = 0.075$ for models with $M_{\rm tot} \le 2.9\ M_\odot$ and $s = 0.1$ for models with $M_{\rm tot} > 2.9\ M_\odot$.

The above phenomenological introduction of nonlinear effects leads to more accurate fits of the initial phases of the secondary components. We note after $\approx$1.0 ms from the onset of the postmerger phase that the evolution is close to quasilinear (linear plus quasilinear combination tones) and the analytic model of Eq. (2) is sufficient for its description.

To summarize, the complete analytic model of the + polarization of the signal amplitude reads

$$h_+^{\rm Fit}(t) = \mathcal{N} \cdot \left(h_+^{\rm peak}(t) \cdot \mathcal{W}(t; s) + \sum_i h_+^i(t) \right), \quad \text{for } i = \text{spiral}, 2 \pm 0, \tag{5}$$

where $h_+^i(t) = A_i e^{(-t/\tau_i)} \cdot \sin(\phi_i(t))$.

To obtain the cross polarization $h_\times^{\rm Fit}(t)$, we adopt the parameters for the amplitudes, damping timescales and frequencies from $h_+^{\rm Fit}(t)$ and assume a phase shift of 90° to the individual initial phases ϕ_i (for $i =$ peak, spiral, 2 ± 0).

B. Semianalytic model

The semianalytic model differs from the analytic model by the substitution of $\phi_{\rm peak}(t)$ with the numerical phase $\phi_{\rm peak}^{\rm numerical}(t)$. The latter is obtained by first extracting the

instantaneous frequency $f_{\rm peak}^{\rm spectrogram}(t)$ from the spectrograms, which is then integrated in time to obtain the phase at a particular time step t_i as $\phi_{\rm peak}^{\rm numerical}(t)$ using the iterative formula

$$\phi_{i+1} = \phi_i + 2\pi f_{{\rm peak},i} \cdot (t_{i+1} - t_i), \tag{6}$$

where $\phi_i \equiv \phi(t = t_i)$ and $f_{{\rm peak},i} \equiv f_{\rm peak}(t = t_i)$. The initial phase $\phi_{\rm peak,0} \equiv \phi(t = 0)$ is a parameter (like $\phi_{\rm peak}$ in the analytic model).

In Sec. VIII we consider an extended semianalytic model, which includes time-dependent secondary components $f_{2\pm0}(t)$ where the phases $\phi_{2\pm0}(t)$ are extracted from the spectrograms in a similar way.

C. Parameter extraction procedure

This subsection is structured as follows: In Sec. V C 1 we discuss the analytic description of $f_{\rm peak}(t)$. In Sec. V C 2 we describe how we obtain the secondary frequencies $f_{\rm spiral}$, $f_{2\pm0}$, and $f_{{\rm spiral}-0}$ from GW spectra. In Sec. V C 3 we describe the method for the extraction of model parameters (A_i, τ_i for $i = {\rm spiral}, 2 \pm 0$) of the secondary components. In Sec. V C 4 we discuss the determination of the remaining parameters $A_{\rm peak}$, $\tau_{\rm peak}$, $\mathcal{N}$, and ϕ_i for $i = {\rm peak}, {\rm spiral}, 2 \pm 0$ and the fit to the simulation data. For all models of our mass sequence we proceed as follows.

1. Analytic description of $f_{\rm peak}(t)$

As mentioned before, we extract the evolving $f_{\rm peak}(t)$ from spectrograms as the frequency of the maximum wavelet coefficient at time t. We parametrize $f_{\rm peak}(t)$ as two-segment piecewise function Eq. (1). We obtain the parameters $[\zeta_{\rm drift}, f_{\rm peak,0}, t_*]$ from a fit to the extracted $f_{\rm peak}(t)$. The fit is done in one step using the analytic function of Eq. (1). The extracted parameters are finally inserted to the analytic model via $\phi_{\rm peak}(t)$ as in Eq. (3).

2. Secondary frequency peaks

We compute the secondary frequencies $f_{\rm spiral}$ and $f_{2\pm0}$ in two steps. First we obtain a rough estimate of the ranges of the different components, which is necessary to correctly identify the different features. Then we pick the frequency at the maximum in the GW spectrum within the estimated frequency ranges of the different components. For the estimate of $f_{\rm spiral}$ we use the rest-mass density profiles on the equatorial plane (as done in [37]). We estimate of $f_{2\pm0}$ using the relation $f_{2\pm0} \approx f_{\rm peak} \pm f_0$. We replace $f_{\rm peak}$ by the mean value of $f_{\rm peak}(t)$ during the first milliseconds, while f_0 is the dominant frequency peak in the Fourier transform of the minimum lapse function $\alpha_{\rm min}$ (see Fig. 7). We note that our choices are in agreement with the empirical relations in [112].

3. Amplitudes A_i and decay timescales τ_i for secondary components

We describe the technique to estimate the amplitudes $A_{\rm spiral}$ and $A_{2\pm0}$ and timescales $\tau_{\rm spiral}$ and $\tau_{2\pm0}$ using the spectrograms. We find that the following procedure leads to results which better reproduce the secondary frequency peaks in GW spectrum.

First we employ spectrograms and extract the wavelet coefficients as functions of time t for the frequency components $f_{\rm spiral}$ and $f_{2\pm0}$ and obtain $\mathcal{A}_{\rm spiral}(t)$ and $\mathcal{A}_{2\pm0}(t)$. We then assume a signal of the form $A_i e^{-t/\tau_i} \cos(2\pi f_i \cdot t)$ and consider each component separately. Within a curve fitting procedure we compute the coefficients at f_i of this model's signal and determine A_i and τ_i such that the coefficient function matches the extracted $\mathcal{A}_i(t)$. The curve fitting procedure adopts a trust-region-reflective algorithm [113–115].

By this method the various components are treated independently; thus in the case of overlapping frequencies the method loses accuracy, since each component is amplified by its neighboring component. The scheme may thus overestimate the amplitudes A_i. To compensate this, we introduced the aforementioned normalization factor $\mathcal{N}$, which we determine in the next step.

4. Fit to simulation data

In the final step we determine the remaining parameters $A_{\rm peak}$, $\tau_{\rm peak}$, and ϕ_i for $i = {\rm spiral}, 2 \pm 0, \mathcal{N}$. We perform a fit of the analytic model to the simulation data, using the aforementioned curve fitting routine, employing a trust-region-reflective algorithm. The previously determined parameters are inserted in the analytic model.

We found that the secondary features of the signal are better reproduced from the spectrograms as described in Sec. VII B, whereas the $f_{\rm peak}$ feature as the dominant component is well determined by the fitting routine.

VI. PERFORMANCE OF THE ANALYTIC AND SEMIANALYTIC MODELS

In this section, we discuss fits of the analytic and semianalytic models to the GW signals extracted from simulations and quantify their performances. We compare the fits to the actual numerical waveform in the time and frequency domains and examine how well certain GW features are reproduced.

We evaluate the performance of the models with the (noise-weighted) FF defined by

$$\mathrm{FF} \equiv \frac{(h_1, h_2)}{\sqrt{(h_1, h_1)(h_2, h_2)}}, \tag{7}$$

using the noise-weighted inner product (h_1, h_2) between two waveforms given by

$$(h_1, h_2) \equiv 4\mathrm{Re} \int_0^\infty df \frac{\tilde{h}_1(f) \cdot \tilde{h}_2^*(f)}{S_h(f)}, \tag{8}$$

where $S_h(f)$ is the detector's noise spectral density and $\tilde{h}_i(f)$ is the Fourier transform of the waveform $h_i(t)$ (for $i = 1, 2$).

Moreover, we consider simpler versions of our analytic model, where we include only a subset of GW features. By this we assess the significance of the individual components of the GW signal.

A. GW fits

First we focus on the analysis of the reference simulation ($M_{\mathrm{tot}} = 2.5\ M_\odot$) and later extend the discussion to the whole sequence of models.

1. Reference simulation

We extract the parameters of the analytic model, Eq. (5) for our reference simulation, as described in Sec. V C. We compare the simulation data to the analytic model in the time domain in Fig. 8. The two signals agree very well throughout the whole postmerger evolution of 24 ms. In the early phase, the dominant and the secondary components are significant, whereas during the later evolution only the f_{peak} component is present. We remark the importance of a time-dependent $f_{\mathrm{peak}}(t)$, which simultaneously yields a proper description of the early and the late phase. Note that the model captures the phase evolution very well at late times.

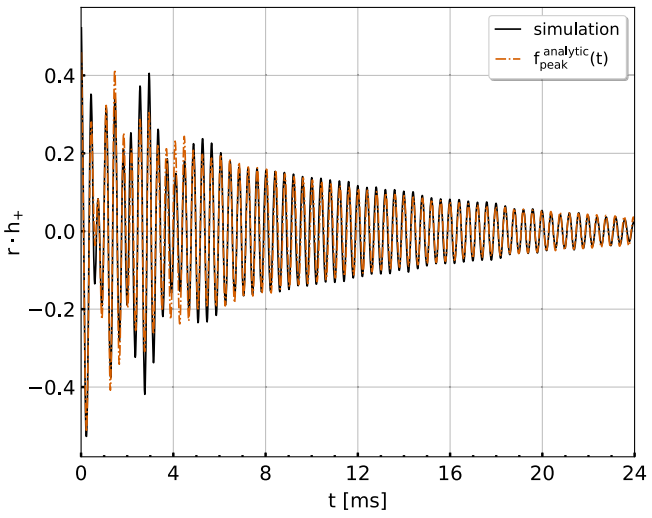

FIG. 8. GW strain $r \cdot h_+(t)$ for the reference simulation and for the analytic model $h_+^{\mathrm{Fit}}(t)$ of Eq. (5).

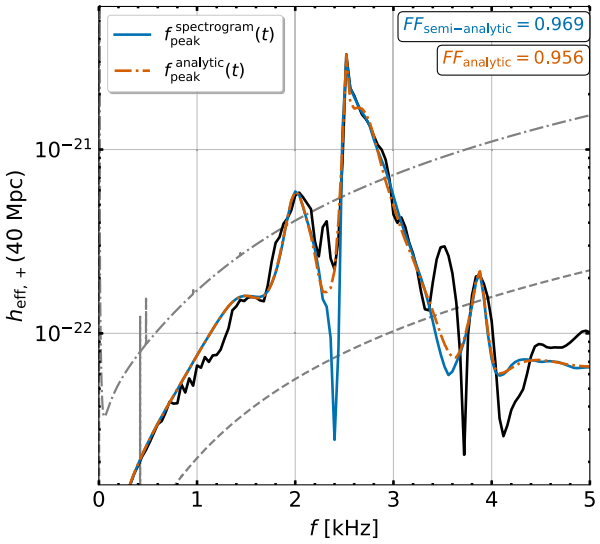

FIG. 9. Postmerger effective GW spectra $h_{\mathrm{eff},+}(f)$ for the numerical simulation (black line), for the analytic model $h_+^{\mathrm{Fit}}(t)$ (orange dashed line) and for the semianalytic model (cyan line; see text), for the reference simulation. Colored boxes indicate the respective FFs.

The success of the analytic model is also seen in the GW spectrum $h_{\mathrm{eff}}(f)$ (see Fig. 9). The analytic model reproduces remarkably well the one-sided f_{peak} structure.

We further assess the time evolution of $f_{\mathrm{peak}}(t)$ and its analytic model of a two-segment piecewise linear function $f_{\mathrm{peak}}^{\mathrm{analytic}}(t)$, Eq. (1). To this end we generate the semianalytic model, as described in Sec. V B. That is, we extract $f_{\mathrm{peak}}^{\mathrm{spectrogram}}(t)$ from the spectrogram and insert the numerical phase $\phi_{\mathrm{peak}}(t)$ using Eq. (6) in the analytic function Eq. (5), whereas we obtain all other parameters as described in Sec. V C. The resulting GW spectra are displayed in Fig. 9 and are compared to the numerical waveform from the simulation. Both models yield spectra that are very close to the spectrum of the numerical simulation. We quantify the accuracy of the models by calculating their fitting factors (with respect to the numerical simulation) assuming the projected ET sensitivity curve [109]. We find fitting factors of FF = 0.969 for the semianalytic model and FF = 0.956 for the analytic model. The semianalytic model yields a slightly higher FF than the analytic model, which is expected since the former contains more precise information about the f_{peak} component. However, the small difference of only 1.34% between the fitting factors of the two models demonstrates that using the analytic model $f_{\mathrm{peak}}^{\mathrm{analytic}}$ instead of the numerically extracted $f_{\mathrm{peak}}^{\mathrm{spectrogram}}(t)$ is sufficient for the description of the time evolution of the $f_{\mathrm{peak}}(t)$ component.

Figure 9 also demonstrates that both the analytic and semianalytic models successfully reproduce the triplet of

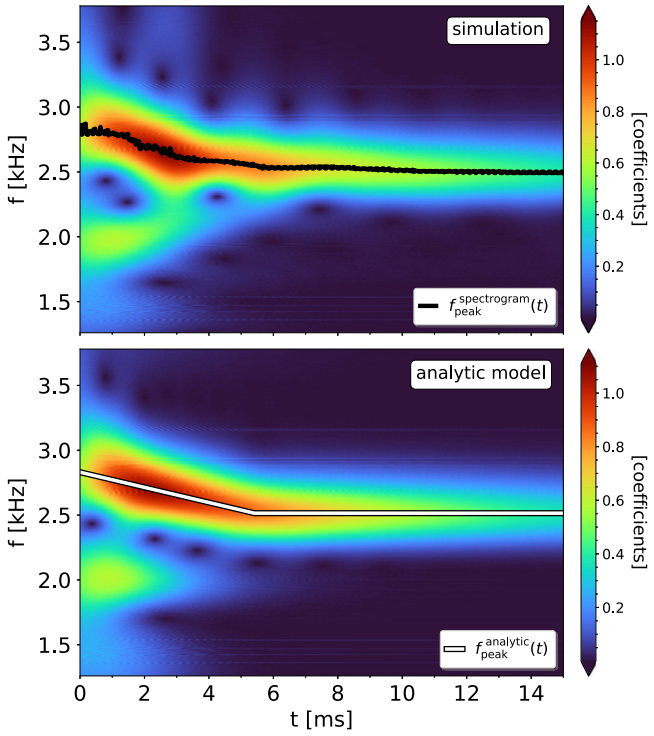

FIG. 10. Top panel: spectrogram of $h_+(t)$ for the reference simulation. The black line corresponds to the numerically extracted $f_{peak}^{spectrogram}(t)$ as described in Fig. 1. Bottom panel: spectrogram of $h_+^{Fit}(t)$ for the reference simulation. The white line illustrates $f_{peak}^{analytic}(t)$.

secondary frequencies f_{spiral} and $f_{2\pm0}$, which implies that our fitting procedure yields reasonable estimates of the corresponding parameters A_i and τ_i. We note that for the purpose of detectability, the secondary peak f_{2-0} is more important than f_{2+0}. Nevertheless, the inclusion of f_{2+0} makes the analytic model more complete and increases the quality of the fit, since the absence of a frequency component in the early phase may spoil the determination of the other parameters. For similar reasons, we found the inclusion of the phenomenological Tukey window function $\mathcal{W}(t;s)$ for the f_{peak} component to be useful.

We note that our model does not include and hence does not reproduce the additional frequency peak at 3.5 kHz in Fig. 9, which remains to be explained and modeled.

Figure 10 directly compares the spectrogram of the simulation (upper panel) and of the analytic model (lower panel). We observe a very good agreement considering the simplicity of the analytic model.

2. Fitting factors along the whole sequence of merger simulations

We test the performance of the analytic model along the sequence of models with different M_{tot} (as defined in Sec. II) and display the spectra for the analytic fits (in comparison to the numerical spectra) in Fig. 11. We find that the analytic model performs well for all configurations and achieves FFs (assuming the sensitivity curve of ET [109]) in the range [0.955, 0.979] for all but the most

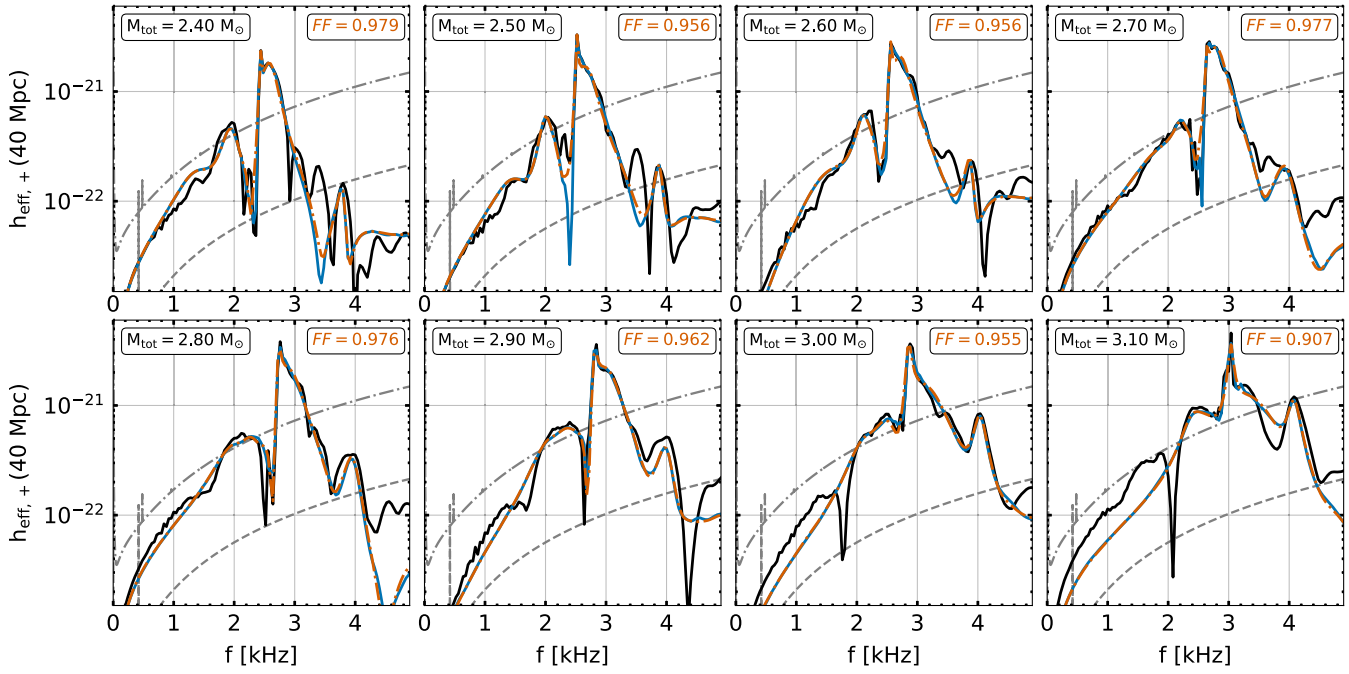

FIG. 11. Postmerger effective GW spectra $h_{eff,+}(f)$ for the simulations (black lines), for the analytic model (orange dashed line), and the semianalytic model (cyan line) along the whole sequence of models. The FFs for the analytic model are reported in each case. Note that for the highest-mass model with $M_{tot} = 3.1\ M_\odot$ an extended analytic model is introduced in Sec. VIII, where a higher FF is achieved.

massive model of this sequence.[1] For the latter model (which is close to the threshold for prompt collapse) we introduce an extended analytic model in Sec. VIII and achieve a comparable fitting factor of 0.962.

In the spectra of Fig. 11, the secondary frequency components are well reproduced by the analytic model and the shape of the frequency peaks agrees with that obtained from the simulations. Our fitting procedure, as described in Sec. V C, yields parameter values that capture well the secondary peaks, except for the amplitude of the f_{2+0} combination tone, A_{2+0}. The latter would need to be individually amplified at the end of the above fitting procedure for models with $M_{\rm tot} \geq 2.8\ M_\odot$, in order to obtain better agreement with the simulations.

B. Simplified analytic models

To further assess our analytic model we consider simplified analytic models and quantify their performance using FFs. We first discuss the reference simulation and then extend the considerations to the whole sequence of merger simulations.

1. Definitions of the simplified analytic models

We consider three simplified analytic models. The first one includes only the time-dependent $f_{\rm peak}(t)$ component and the second includes the $f_{\rm peak}(t)$ component plus one secondary component. As before, the $f_{\rm peak}(t)$ component is modeled by the analytic two-segment function $f_{\rm peak}^{\rm analytic}(t)$. For low-mass models, including the reference simulation, the dominant secondary component is the $f_{\rm spiral}$, while for higher-mass configurations f_{2-0} becomes the most prominent feature. In the third model, $f_{\rm peak}(t)$ is kept constant and equal to $f_{\rm peak} = \langle f_{\rm peak}^{t\in[0,t_*]} \rangle$, while all the secondary frequency components are included.

We note that for the two-component model (one secondary component) we do not employ the normalization factor $\mathcal{N}$. For the one-component model we discard the phenomenological window $\mathcal{W}(t;s)$, since this leads to a slightly higher fitting factor in this case.

Table I summarizes information on the various analytic, semianalytic and simplified models and their assigned names.

2. Fitting factors for the reference simulation

We perform the fits using the aforementioned procedure for the complete analytic model (Ac), the two-component analytic model (A2), and the one-component analytic model (A1) and display the corresponding postmerger GW spectra in Fig. 12 for the reference simulation. All three models reproduce well the shape of the $f_{\rm peak}$ peak, since they include the time-dependent description for $f_{\rm peak}^{\rm analytic}(t)$. However, there are significant differences in the FFs. The complete analytic model achieves FF = 0.956. As one would expect, the fewer components are included in the model, the worse the value of the fitting factor. The two-component model achieves FF = 0.931, whereas for the one-component model the performance deteriorates to FF = 0.825.

To further understand the impact of differences in the achieved fitting factors we convert them to the reduction in

TABLE I. Definitions for the various analytic, semianalytic and simplified models that we consider. When the time dependence is explicitly written, a time-dependent description is employed for that particular component.

Model description	Name	Included components
Complete analytic model	Ac	$f_{\rm peak}^{\rm analytic}(t)$, $f_{\rm spiral}$, f_{2-0}, f_{2+0}
Complete semianalytic model	Sc	$f_{\rm peak}^{\rm spectrogram}(t)$, $f_{\rm spiral}$, f_{2-0}, f_{2+0}
Simplified (two-component) analytic model	A2	$f_{\rm peak}^{\rm analytic}(t)$, $f_{\rm spiral}$ or f_{2-0}
Simplified (one-component) analytic model	A1	$f_{\rm peak}^{\rm analytic}(t)$
Simplified (const. frequencies) complete analytic model	sAc	$\langle f_{\rm peak}^{t\in[0,t_*]} \rangle$, $f_{\rm spiral}$, f_{2-0}, f_{2+0}

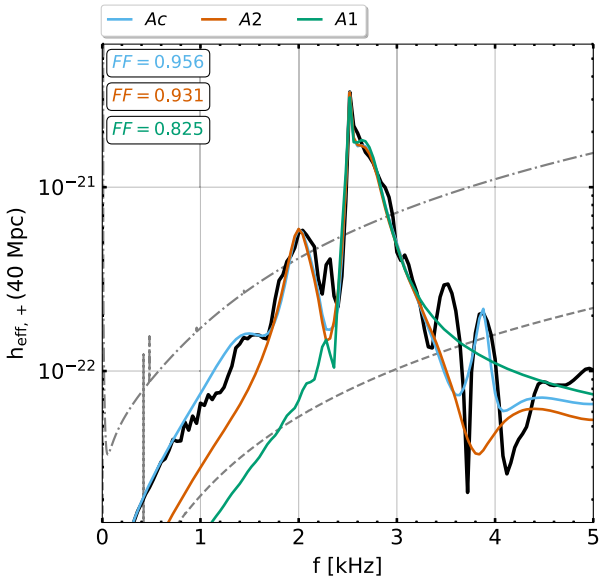

FIG. 12. Postmerger effective GW spectra $h_{\rm eff,+}(f)$ for the simulation (black lines) and for three analytic models, Ac (cyan line), A2 (orange line) and A1 (green line) for the reference simulation. In each case, the corresponding FF is shown.

[1]As for the reference simulation, we obtain only slightly better FFs for the semianalytic model—even for the most massive model—and hence we only report the FFs for the analytic model along the whole sequence.

detection rates, which is considered to scale as $(1 - \mathrm{FF}^3) \times 100$ [116]. For the reference simulation discussed in Fig. 12, the complete analytic model achieves a reduction of the detection rate of only 12.63%, whereas the simpler, two-component and one-component analytic models suffer from larger reductions of 19.30% and 43.85%, respectively.

The above comparison quantifies the importance of including at least one secondary component to the analytic description of the postmerger phase, as this significantly increases the detectability of the signal with matched-filtered techniques; otherwise, more than half of the candidate events would go undetected.

3. Phase evolution

We compare the analytic model fits with respect to the gravitational phase $\phi(t)$ defined by

$$\phi(t) = -\arctan\left(\frac{h_\times(t)}{h_+(t)}\right). \tag{9}$$

We compute the phase difference $\Delta\phi(t) = \phi^{\mathrm{fit}}(t) - \phi^{\mathrm{simulation}}(t)$ between the analytic models and the GW signal from the simulation (see Fig. 13). In the following analysis, we also consider the complete semianalytic model (Sc) where the $f_{\mathrm{peak}}(t)$ component is modeled by $f_{\mathrm{peak}}^{\mathrm{spectrogram}}(t)$. We split the postmerger signal in two phases: the initial phase, which lasts approximately 8 ms, and the late phase referring to the rest of signal.

In the early phase, the phase differences $\Delta\phi(t)$ are characterized by low-amplitude spikes. These spikes are present in all of the analytic models. The semianalytic model follows the same trends, although with slightly lower amplitudes. In the late postmerger phase, the phase difference for the analytic models is dominated by $f_{\mathrm{peak}}^{\mathrm{analytic}}(t)$, since by that time the secondary peaks have practically diminished. The semianalytic model has a notably different phase evolution than the analytic models, although the absolute value $|\Delta\phi(t)|$ is comparable.

4. Fitting factors along the whole sequence of merger simulations

We compare the fitting factors achieved by the complete analytic (Ac) and semianalytic (Sc) models and by the simplified analytic models (A2 and A1) along the whole sequence of merger simulations in Fig. 14 and report the corresponding reduction in detection rates in Table II. The general trend is consistent with the findings for the reference simulation. The complete analytic and semianalytic models perform best leading to the highest fitting factors. The fitting factors for the simple, one-component analytic model are between 0.82 and 0.86 for most simulations but deteriorate drastically for the two highest-mass simulations, leading to a reduction of the detection rate of up to 72.28%. The two-component model performs significantly better than the one-component model, but it is still insufficient, when compared to the complete analytic or semianalytic models. We thus conclude that postmerger GW templates should include several secondary components such as f_{spiral} and $f_{2\pm0}$, if a small reduction of the detection is to be achieved.

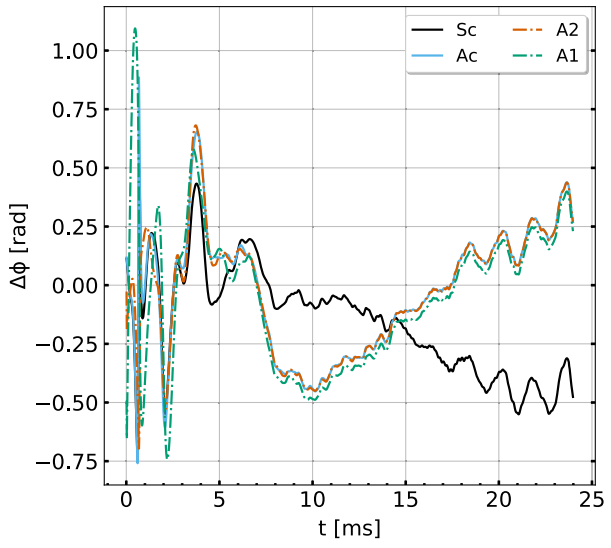

FIG. 13. Gravitational phase difference $\Delta\phi(t)$ between simulation and analytic or semianalytic model fits for the reference simulation in postmerger phase.

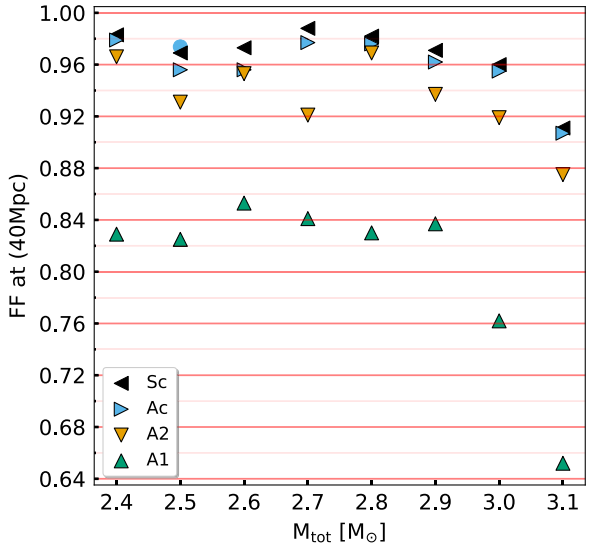

FIG. 14. FFs for the analytic, and semianalytic model fits for a source at polar distance of 40 Mpc using the Einstein Telescope sensitivity curve [109]. The blue circle displays the FF for the Ac model fit for the HR simulation (see Appendix A 2).

TABLE II. Reduction in detection rates for various analytic and semianalytic models. The definition of each model is given in Table I.

	Reduction in detection rates (%)			
$M_{\rm tot}$ $[M_\odot]$	Sc	Ac	A2	A1
2.4	5.01	6.17	9.86	43.03
2.5	9.01	12.63	19.30	43.85
2.6	7.88	12.63	13.45	37.93
2.7	3.56	6.74	21.88	40.52
2.8	5.30	7.03	9.01	42.82
2.9	8.45	10.97	17.73	41.36
3.0	11.53	12.90	22.38	55.75
3.1	24.39	25.39	33.01	72.28

5. *Importance of the two-segment description of $f_{\rm peak}(t)$*

Furthermore, we assess the significance of the time-dependent description of $f_{\rm peak}(t)$ in the analytic model in comparison to the constant frequency description. We consider the simplified complete analytic model (sAc) where $f_{\rm peak}(t)$ is constant and equal to $f_{\rm peak} = \langle f_{\rm peak}^{t\in[0,t_*]} \rangle$, and we perform the fits for the models Ac, sAc and compare the FFs.

Table III and Fig. 15 (top panel) show the fitting factors along the mass sequence. The model sAc leads to small FFs, ranging from 0.727 to 0.846. In contrast, the Ac model performs significantly better. In terms of the reduction in detection rates, the sAc model is significantly worse than the Ac model. We note that for the two highest-mass models ($M_{\rm tot} = 3.0, 3.1\ M_\odot$) substituting $\langle f_{\rm peak}^{t\in[0,t_*]} \rangle$ with $f_{\rm peak}$ leads to FFs close to the ones obtained with Ac.

VII. PARAMETERS OF THE ANALYTIC MODEL

In this section we discuss the parameters of the analytic model and their dependence on the total binary mass $M_{\rm tot}$.

TABLE III. FFs and reduction in detection rates (%) for the Ac and sAc analytic models for the postmerger GW emission (see Table I for definitions).

	FFs		Reduction in detection rates (%)	
$M_{\rm tot}$ $[M_\odot]$	Ac	sAc	Ac	sAc
2.4	0.979	0.827	6.17	43.44
2.5	0.956	0.727	12.63	61.58
2.6	0.956	0.773	12.63	53.81
2.7	0.977	0.845	6.74	39.66
2.8	0.976	0.846	7.03	39.45
2.9	0.962	0.824	10.97	44.05
3.0	0.955	0.779	12.90	52.73
3.1	0.907	0.797	25.39	49.37

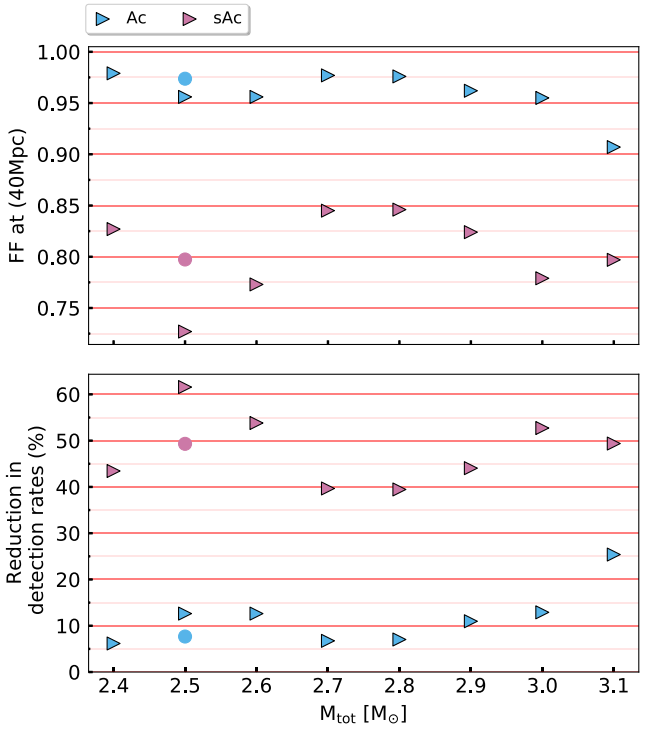

FIG. 15. Top panel: FFs for the Ac and sAc analytic fits. Bottom panel: reduction in detection rates for the Ac and sAc analytic fits. The circles indicate the FF (blue) and reduction in detection rates (pink) for the sAc model fit for the HR simulation (see Appendix A 2).

We find a systematic dependence on $M_{\rm tot}$ for all the parameters of the model and employ polynomial fits to obtain analytic descriptions of the respective dependencies. We first focus on the analytic description of $f_{\rm peak}(t)$ and the parameters which determine the two-segment piecewise function, Eq. (1). We then discuss the amplitudes A_i, timescales τ_i and normalization factor $\mathcal{N}$. We address the initial phases ϕ_i where we find additional correlations between these parameters. Finally, we employ empirical relations for all the parameters of the analytic model (Ac) and discuss a purely analytic model which uses exclusively analytic functions.

A. $f_{\rm peak}(t)$ parametrization

Figure 16 shows the extracted parameters $\zeta_{\rm drift}$, t_*, and $f_{\rm peak,0}$ as functions of total mass $M_{\rm tot}$ for our sequence of simulations. We find that these parameters follow specific dependencies. The dependence of the parameters $t_*, f_{\rm peak,0}$ and $\zeta_{\rm drift}$ can be modeled by second- and third-order polynomials (black lines), respectively, given by

$$\zeta_{\rm drift} = -1.420 \cdot M_{\rm tot}^3 + 11.085 \cdot M_{\rm tot}^2 - 28.834 \cdot M_{\rm tot} + 24.943, \quad (10)$$

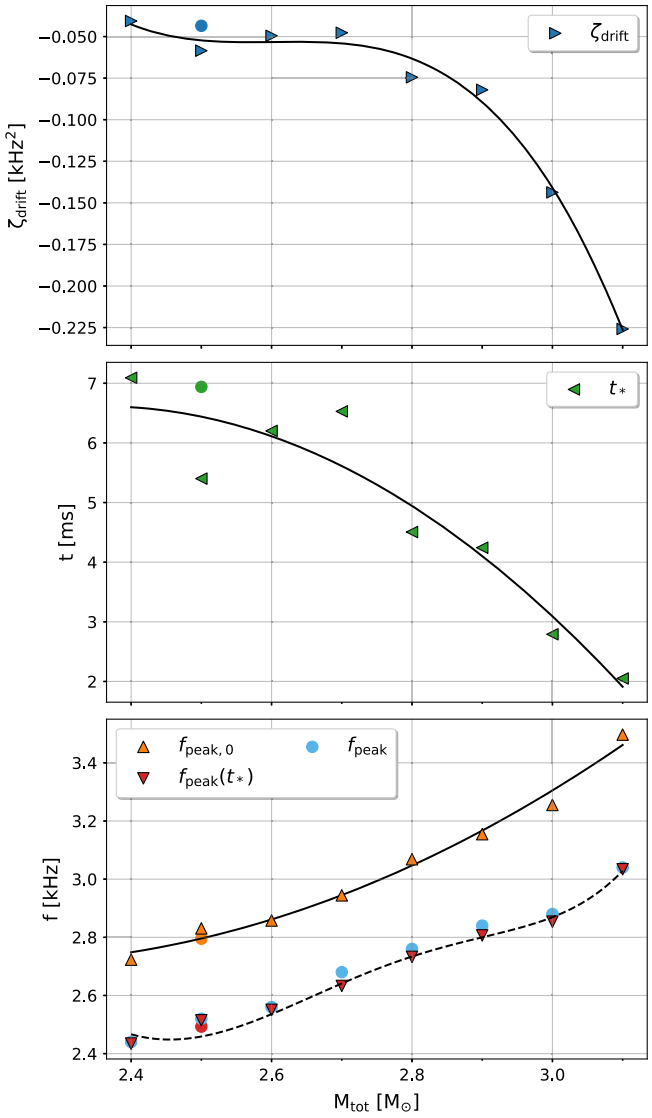

FIG. 16. Top panel: $\zeta_{\rm drift}$ parameter along the mass sequence. The black curve shows a third-order polynomial fit. Middle panel: t_* parameter along the mass sequence. The black curve shows a second-order polynomial fit. Bottom panel: $f_{\rm peak,0}$ parameter (orange) along the mass sequence. The black solid curve shows a second-order polynomial fit. In addition, data points (red) along the mass sequence are shown for $f_{\rm peak}(t_*)$, which is determined by $\zeta_{\rm drift}$, $f_{\rm peak,0}$, and t_*. The black dashed curve is determined by polynomial fits to $\zeta_{\rm drift}$, $f_{\rm peak,0}$, and t_*. Cyan circles indicate the $f_{\rm peak}$ extracted from the GW spectra (see Fig. 5). The rest of the circles indicate the respective parameters (for each figure) for the HR simulation (see Appendix A 2).

$$f_{\rm peak,0} = +0.908 \cdot M_{\rm tot}^2 - 3.974 \cdot M_{\rm tot} + 7.058, \quad (11)$$

$$t_* = -8.523 \cdot M_{\rm tot}^2 + 40.179 \cdot M_{\rm tot} - 40.741. \quad (12)$$

Figure 16 (bottom) shows the final frequency $f_{\rm peak}(t = t_*)$, which by definition is determined by the parameters $\zeta_{\rm drift}$, $f_{\rm peak,0}$, and t_* [the black dashed curve is determined by Eqs. (10)–(12)].

The parameter $f_{\rm peak}(t_*)$ (see Fig. 16) approximately coincides with $f_{\rm peak}$ (maximum of the peak in the GW spectra) and increases with the total mass $M_{\rm tot}$ (since the remnant becomes more compact). $f_{\rm peak,0}$ exhibits a similar dependence on the total mass $M_{\rm tot}$. As previously mentioned, $f_{\rm peak}(t)$ evolves faster and more significantly for high-mass configurations. This is confirmed by the difference $\Delta f_{\rm peak} = f_{\rm peak,0} - f_{\rm peak}(t_*)$, which increases with total mass $M_{\rm tot}$ from 0.288 kHz for the model with the lowest mass to 0.462 kHz for the configuration with $M_{\rm tot} = 3.1\ M_\odot$.

The duration of the frequency drift, t_*, is a decreasing function of the total binary mass $M_{\rm tot}$. We note that in particular t_* possibly exhibits a dependence on the numerical scheme, resolution and physics of the simulation tool, which can affect the angular momentum redistribution of the remnant and possibly prolong or shorten the drift.

The slope parameter $\zeta_{\rm drift}$ is approximately constant (≈ -0.060 kHz^2) for $M_{\rm tot} \leq 2.8\ M_\odot$. However, a rapid decrease occurs as the total mass $M_{\rm tot}$ approaches $M_{\rm thres}$ (see Fig. 16). Such a trend may not be unexpected as a result of an accelerated evolution of the remnant (in the early postmerger phase) due to the strong gravity.

If it is possible to extract $\zeta_{\rm drift}$, t_* and $\Delta f_{\rm peak}$, one may use this information to estimate the proximity to a prompt collapse. To this end, the occurrence of a faster frequency evolution for high-mass binaries should be confirmed for other EOS models, possibly considering $\zeta_{\rm drift}$, t_*, and $\Delta f_{\rm peak}$ relative to $f_{\rm peak}$, instead of absolute values.

B. Amplitudes, timescales, normalization factor

In this subsection we discuss the properties of the dominant component's parameters $A_{\rm peak}$ and $\tau_{\rm peak}$, the parameters of the secondary components $A_{\rm spiral}$, $A_{2\pm0}$, $\tau_{\rm spiral}$, and $\tau_{2\pm0}$ and the normalization factor $\mathcal{N}$. We employ the parameters determined for the complete analytic model (Ac).

1. $A_{\rm peak}$ and $\tau_{\rm peak}$

Figures 17(a) and 17(b) show the parameters $A_{\rm peak}$ and $\tau_{\rm peak}$. These parameters follow dependencies, which can be modeled by second-order polynomial fits given by

$$A_{\rm peak} = -0.409 \cdot M_{\rm tot}^2 + 3.657 \cdot M_{\rm tot} - 6.130, \quad (13)$$

$$\tau_{\rm peak} = +7.782 \cdot M_{\rm tot}^2 - 53.040 \cdot M_{\rm tot} + 93.542. \quad (14)$$

$A_{\rm peak}$ increases with $M_{\rm tot}$, which may be expected, since the involved masses are higher and also the initial excitation is more pronounced. $\tau_{\rm peak}$ decreases as the total binary mass $M_{\rm tot}$ increases, indicating a stronger damping.

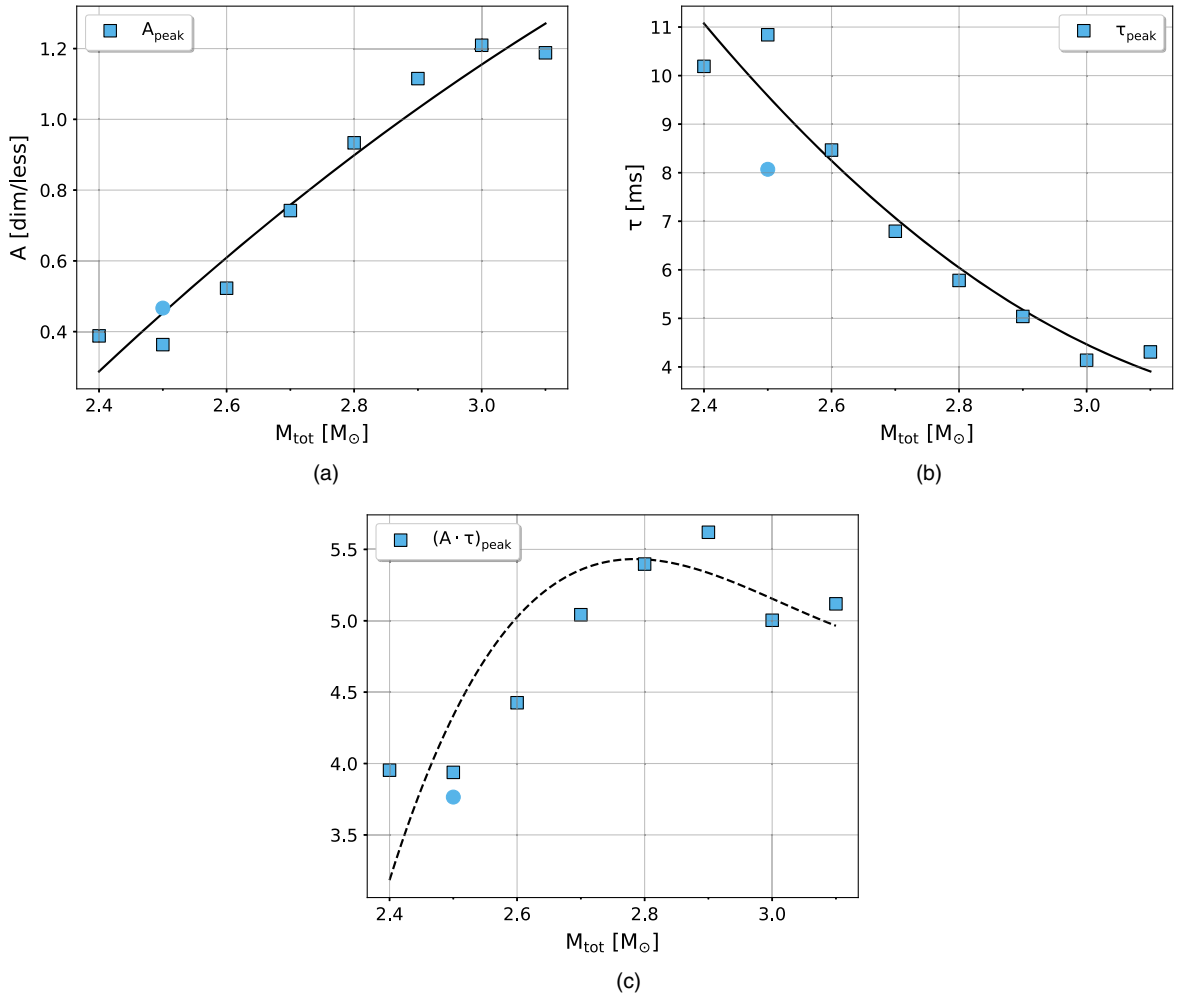

FIG. 17. Top left panel: analytic model dimensionless amplitude $A_{\rm peak}$ for $r \cdot h_+(t)$ for the analytic model which employs the $f_{\rm peak}^{\rm analytic}(t)$ description. The black curve corresponds to second-order polynomial fit. Top right panel: analytic model timescale $\tau_{\rm peak}$ for the analytic model which employs the $f_{\rm peak}^{\rm analytic}(t)$ description. The black curve corresponds to second-order polynomial fit. Bottom panel: analytic model products $(A \cdot \tau)_{\rm peak}$. Black dashed curves determined by fits to $A_{\rm peak}$ and $\tau_{\rm peak}$. The blue circles indicate the respective parameters (for each figure) for the HR simulation (see Appendix A 2).

2. $A_{\rm spiral}$, $A_{2\pm0}$, $\tau_{\rm spiral}$, and $\tau_{2\pm0}$

Figures 18(a) and 18(b) display the parameters A_i and τ_i (for $i = \text{spiral}, 2 \pm 0$). The amplitudes A_i and timescales τ_i correlate with the total mass $M_{\rm tot}$ and follow specific trends. We quantify these dependencies by performing second-order polynomial fits resulting in

$$\tau_{\rm spiral} = -0.874 \cdot M_{\rm tot}^2 + 3.521 \cdot M_{\rm tot} - 2.005, \quad (15)$$

$$\tau_{2-0} = +2.057 \cdot M_{\rm tot}^2 - 10.804 \cdot M_{\rm tot} + 14.606, \quad (16)$$

$$\tau_{2+0} = +8.469 \cdot M_{\rm tot}^2 - 48.785 \cdot M_{\rm tot} + 71.671, \quad (17)$$

$$A_{\rm spiral} = +2.649 \cdot M_{\rm tot}^2 - 13.580 \cdot M_{\rm tot} + 17.752, \quad (18)$$

$$A_{2-0} = -1.704 \cdot M_{\rm tot}^2 + 10.004 \cdot M_{\rm tot} - 13.909, \quad (19)$$

$$A_{2+0} = +0.816 \cdot M_{\rm tot}^2 - 3.920 \cdot M_{\rm tot} + 4.734. \quad (20)$$

These relations are not particularly tight, especially for A_{2-0} and $\tau_{\rm spiral}$, which is likely caused by the difficulty to precisely extract secondary features from the complex signal. However, the amplitudes of all secondary features clearly increase with mass.

As the total mass $M_{\rm tot}$ increases, the components $f_{2\pm0}$ become more prominent and this is seen in $A_{2\pm0}$ too [see Fig. 18(a)]. This is understandable, because the radial oscillation mode is more strongly excited for high-mass models. For low-mass configurations, the coupling to the radial oscillation is significantly suppressed (see Fig. 6), and consequently the amplitudes of the couplings f_{2-0} and f_{2+0} should be small, which is only the case for the f_{2+0} component. We suspect that the relatively high amplitude

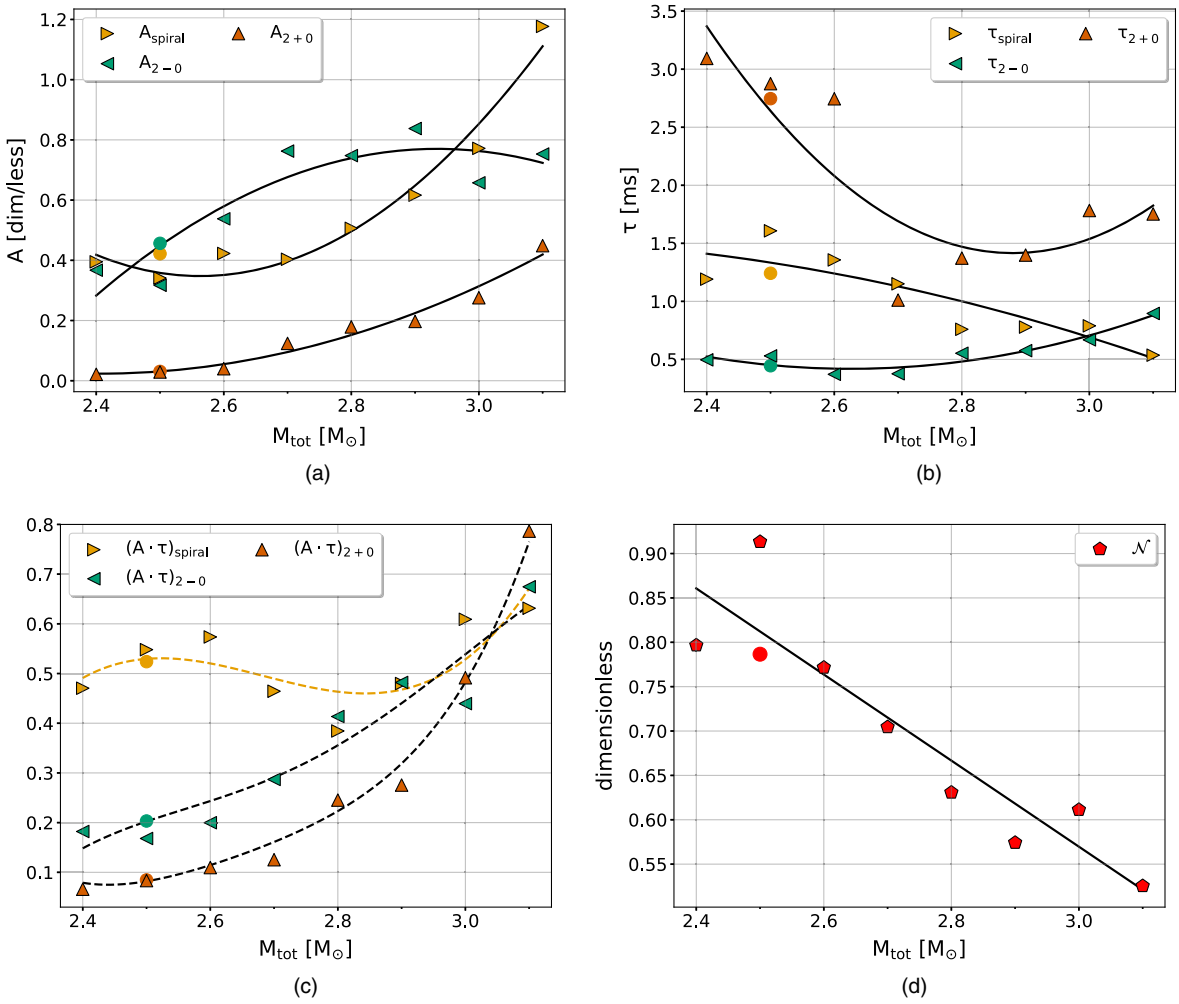

FIG. 18. Top left panel: analytic model dimensionless amplitudes $A_{\rm spiral}$, A_{2-0}, and A_{2+0} for $r \cdot h_+(t)$ extracted from spectrograms. Black curves correspond to second-order polynomial fits. Top right panel: analytic model timescales $\tau_{\rm spiral}$, τ_{2-0}, and τ_{2+0} extracted from spectrograms. Black curves correspond to second-order polynomial fits. Bottom left panel: analytic model products $(A \cdot \tau)_{\rm spiral}$, $(A \cdot \tau)_{2-0}$, and $(A \cdot \tau)_{2+0}$. Black dashed curves determined by polynomial fits to A_i, τ_i for $i =$ spiral, 2 ± 0. The yellow dashed curve corresponds to the fourth-order polynomial fit to $(A \cdot \tau)_{\rm spiral}$. Bottom right panel: analytic model correction factor $\mathcal{N}$ for the analytic model which employs the $f_{\rm peak}^{\rm analytic}(t)$ description. The black curve corresponds to a linear fit. The colored circles indicate the respective parameters (for each quantity and figure) for the HR simulation (see Appendix A 2).

A_{2-0} for small $M_{\rm tot}$ is an artifact of the fit and is compensated by a very small decay timescale. The weakness of the radial oscillation implies that the $\tau_{2\pm0}$ are not very meaningful measures for low-mass systems. For higher total binary masses one can see a mild increase of $\tau_{2\pm0}$, which is in line with the behavior in Fig. 6. The timescales of the spiral component exhibit a mild decrease, corresponding to a faster dissipation of the tidal bulges. The amplitude of the $f_{\rm spiral}$ component similarly increases with $M_{\rm tot}$.

Furthermore, we consider the product $(A \cdot \tau)_i$ as a quantitative measure for the strength of a secondary feature. Figure 18(c) shows the products $(A \cdot \tau)_i$ for each frequency component. We use Eqs. (15)–(20) to derive analytic expressions displayed by dashed curves. The products $(A \cdot \tau)_{2\pm0}$ increase systematically with $M_{\rm tot}$ as expected and closely follow the analytic expressions. The product $(A \cdot \tau)_{\rm spiral}$ is roughly constant.[2]

The strength of the secondary components quantified as in Fig. 18(c) resembles the behavior which was anticipated in [37] and reproduces different types of postmerger GW emission: For low-mass binaries the $f_{\rm spiral}$ component is dominant (type III in the notation of [37]), for intermediate masses the strength of $f_{\rm spiral}$ and f_{2-0} is roughly comparable (type II), and for models with very high $M_{\rm tot}$ the

[2] $(A \cdot \tau)_{\rm spiral}$ shows a large scatter from the derived analytic expression [using Eq. (18) and (15)]; however, we find that a fourth-order polynomial fit describes well the trend.

couplings with the radial oscillation are dominant over $f_{\rm spiral}$ (type I). The products $(A\cdot\tau)_i$ may thus serve as a quantitative measure to classify different types of postmerger dynamics and GW emission including the morphology of the spectrum.

We note that the method we use for the derivation of A_i and τ_i introduces a bias whenever f_{2-0} and $f_{\rm spiral}$ are close (see Sec. VII B). The latter is possibly one of the reasons for the scattering of A_i and τ_i from the analytic fits.

3. $\mathcal{N}$

Figure 18(d) shows the normalization factor $\mathcal{N}$ as a function of total mass $M_{\rm tot}$ for fits with the complete analytic model (Ac). We find a linear dependence on $M_{\rm tot}$ modeled by

$$\mathcal{N} = -0.485\cdot M_{\rm tot} + 2.025. \tag{21}$$

$\mathcal{N}$ becomes less important (close to 1) for low-mass configurations and more significant (close to 0.50) for high-mass configurations.

One reason for this trend may be that for estimating A_i and τ_i we treat each component separately. In low-mass configurations the components $f_{\rm spiral}$ and f_{2-0} are well separated and therefore the parameters A_i and τ_i are accurately derived. However, this is not the case for high-mass configurations, where the peaks overlap, and thus the parameters may be overestimated and the correction becomes necessary.

Another reason may be the fact that the $f_{2\pm0}$ components are significantly weaker than the $f_{\rm spiral}$ components for low-mass systems [see e.g., the products $(A\cdot\tau)_i$]. Hence, their contribution to the total signal is minor and a single secondary feature does not require significant corrections by the normalization factor.

C. Initial phases $\phi_{\rm peak}$, $\phi_{\rm spiral}$, and $\phi_{2\pm0}$

In this subsection we discuss the properties of the initial phases ϕ_i (for $i = {\rm peak, spiral}, 2\pm0$) for all the models in the sequence of simulations. For the analysis we add multiples of 2π to the initial phases ϕ_i such that $\phi_i(M_{\rm tot})$ becomes an increasing function (see Fig. 19).

We find a tight correlation between ϕ_i and the total mass $M_{\rm tot}$. We model this dependence with a two-segment piecewise function consisting of two linear fits which intersect at total mass of $M_{\rm tot} = 2.7\ M_\odot$ (see Appendix C).

These remarkably tight correlations imply that the properties of the gravitational phase $\phi(t)$ [see Eq. (9)] in the early postmerger phase depend systematically on the total mass $M_{\rm tot}$.

Furthermore, we find tight correlations between the initial phases $\phi_{\rm spiral}$, $\phi_{2\pm0}$ and $\phi_{\rm peak}$ as shown in Fig. 20. We model these correlations with linear fits given by

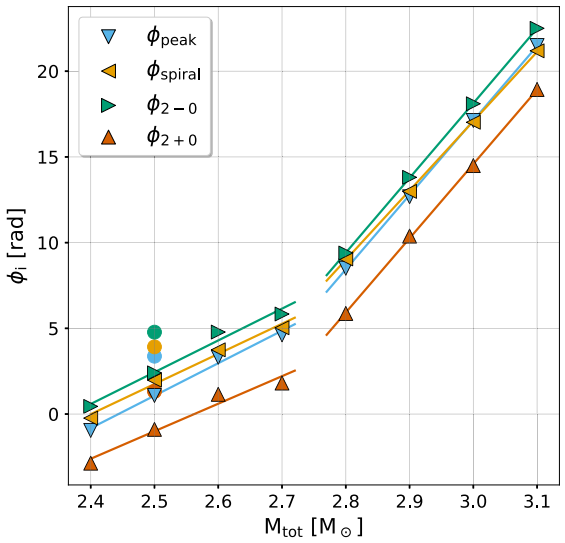

FIG. 19. Initial phases ϕ_i (for $i = $ peak, spiral, 2 ± 0) for the analytic model which employs the $f_{\rm peak}^{\rm analytic}(t)$ description as a function of total binary mass. Colored curves correspond to piecewise linear fits. The colored circles indicate the respective parameters for the HR simulation (see Appendix A 2).

$$\phi_{\rm spiral} = +0.953\cdot\phi_{\rm peak} + 0.756, \tag{22}$$

$$\phi_{2-0} = +0.980\cdot\phi_{\rm peak} + 1.345, \tag{23}$$

$$\phi_{2+0} = +0.975\cdot\phi_{\rm peak} - 2.166. \tag{24}$$

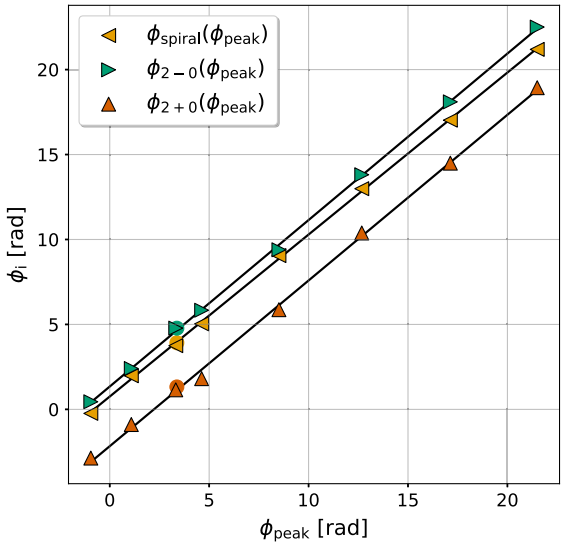

FIG. 20. Initial phases ϕ_i (for $i = $ spiral, 2 ± 0) with respect to $\phi_{\rm peak}$ for the analytic model which employs the $f_{\rm peak}^{\rm analytic}(t)$ description. Black curves correspond to linear fits. The colored circles indicate the respective parameters for the HR simulation (see Appendix A 2).

The slope parameters in Eqs. (22)–(24) are approximately equal and differ at most by 3%. We note that the slopes are also close to 1, which would imply a constant difference in phase between the $f_{\rm peak}$ component and the secondary components. It may well be that these relations and the ones shown in Fig. 19 are in reality even tighter and the small but finite scatter results from finite resolution in the simulations or the fitting procedure. Such tight relations can be employed to reduce the complexity of the analytic fit by reducing the parameter space.

We find that using the $\phi_{\rm peak}(M_{\rm tot})$ and $\phi_{\rm spiral}(\phi_{\rm peak})$, $\phi_{2\pm0}(\phi_{\rm peak})$ relations [see Eqs. (22)–(24)] one may reduce the number of the analytic model's parameters (and thus the complexity of the fitting procedure) and obtain good fits to the data. We test this by substituting the initial phases ϕ_i with the predictions made by Eqs. (C1) and (22)–(24) and find that the FFs only differ by a few percent (0.5%–3%) compared to fits to the analytic model. When we perform a phase alignment in the waveforms the FFs differ by at most $\approx$1%.

We overplot the initial phases ϕ_i (for $i =$ peak, spiral, 2 ± 0) for the HR simulation in Figs. 19 and 20 (see Appendix A 2). These appear to be slightly larger than the ones from the mass sequence simulations; however, their relative difference is similar to the mass sequence simulations as corroborated by Fig. 20.

Furthermore, we also find that these tight correlations between the initial phases [Eqs. (22)–(24)] are unaffected by residual eccentricities in the ID (see Fig. 25 and Appendix A 1).

D. Purely analytic model

We consider a *purely analytic model* $\mathcal{P}(M_{\rm tot}, t)$ which uses the analytic functions Eqs. (10)–(21) and (C1)–(C4) and thus depends only on $M_{\rm tot}$. We evaluate its performance by computing the respective FFs. Table IV shows the FFs for the analytic model $\mathcal{P}(M_{\rm tot}, t)$ compared to the Ac analytic fits. The FFs drop significantly as expected; however, the majority of the fits still result in FFs $\gtrsim 0.80$.

TABLE IV. FFs for the analytic model Ac fits, the purely analytic model $\mathcal{P}(M_{\rm tot}, t)$, and the analytic model with one free parameter $\mathcal{P}(M_{\rm tot}, t; \phi_{\rm peak})$.

	FFs		
$M_{\rm tot}$ $[M_\odot]$	Ac	$\mathcal{P}(M_{\rm tot}, t)$	$\mathcal{P}(M_{\rm tot}, t; \phi_{\rm peak})$
2.4	0.979	0.653	0.801
2.5	0.956	0.795	0.847
2.6	0.956	0.912	0.913
2.7	0.977	0.878	0.922
2.8	0.976	0.878	0.899
2.9	0.962	0.848	0.905
3.0	0.955	0.595	0.864
3.1	0.907	0.887	0.898

The FFs can be further improved by considering an analytic model where $\phi_{\rm peak}$ is treated as a free parameter, denoted by $\mathcal{P}(M_{\rm tot}, t; \phi_{\rm peak})$. In this case, almost all configurations lead to FFs $\gtrsim 0.85$ (see Table IV).

These considerations show that it may be possible to determine the different analytic functions Eqs. (10)–(21) and (C1)–(C4) (or only piecewise linear segments of these functions) by several simulations and anticipated observations and then use those functions to interpolate the model in $M_{\rm tot}$.

VIII. MODELS CLOSE TO PROMPT COLLAPSE

In this section we analyze the spectral properties of configurations with a total mass $M_{\rm tot}$ close to threshold mass for prompt collapse $M_{\rm thres}$. Fitting factors decrease for these high-mass models, which possibly points to an incompleteness of our analytic model. We separately consider two modifications to the analytic model in order to increase the FF. First, we include a dynamical evolution of $f_{2\pm0}(t)$. Second, we incorporate the $f_{\rm spiral-0}$ component, i.e., an additional coupling between $f_{\rm spiral}$ and f_0 (see Sec. III C). Table V summarizes information for the extended analytic models.

A. Extended analytic models and GW fits

To assess the importance of the time evolution of $f_{2\pm0}(t)$, we extracted $f_{2\pm0}(t)$ from spectrograms (see Sec. IV) and inserted the numerically extracted values into the analytic model (see Sec. V B). We do not further discuss a parametrization of $f_{2\pm0}(t)$ because we find below that even the complete numerical description of $f_{2\pm0}(t)$ yields only a minor improvement.

Figure 21 shows the fits to the simulation with total binary mass $M_{\rm tot} = 3.1\ M_\odot$ for the extended analytic models. The introduction of the time-evolving components $f_{2\pm0}(t)$ leads to a mild increase of the fitting factor: ${\rm FF}_{\rm new,1} = 0.916$ compared to the original of ${\rm FF}_{\rm old} = 0.907$ (see Sec. VI A). This increase in FF slightly improves the reduction in detection rates from 25.39% to 23.14%. The model with the dynamical $f_{2\pm0}(t)$ qualitatively reproduces a small peak at approximately 1.9 kHz (orange curve in Fig. 21) but still does not yield a good description of the simulation below 2 kHz.

TABLE V. Definitions for the two extended analytic models. When the time argument is explicitly written, a time-dependent description is employed for that particular component.

Model description	Name	Components
Extended analytic model 1	M1	$f_{\rm peak}^{\rm analytic}(t)$, $f_{\rm spiral}$, $f_{2-0}(t)$, $f_{2+0}(t)$
Extended analytic model 2	M2	$f_{\rm peak}^{\rm analytic}(t)$, $f_{\rm spiral}$, f_{2-0}, f_{2+0}, $f_{\rm spiral-0}$

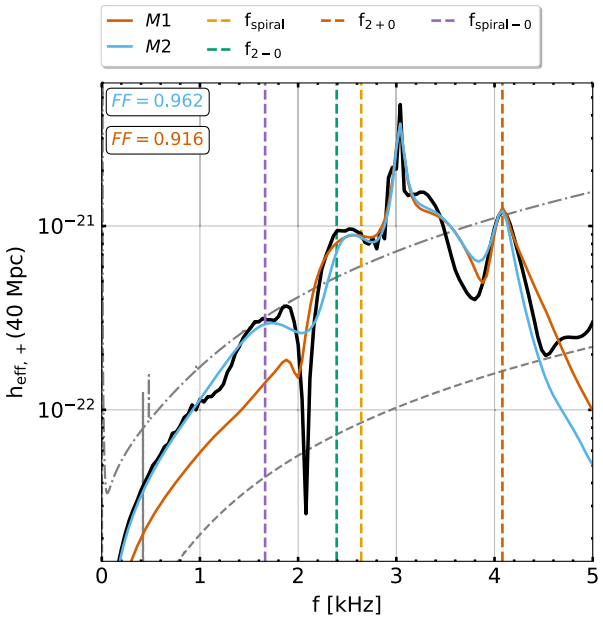

FIG. 21. Effective GW spectra $h_{\mathrm{eff},+}(f)$ for simulation and analytic models for $M_{\mathrm{tot}} = 3.1\ M_{\odot}$ model. The black line corresponds to the simulation. Colored curves illustrate the analytic model fits as described by the labels. Colored boxes show the corresponding FFs. Dashed vertical lines indicate secondary frequencies.

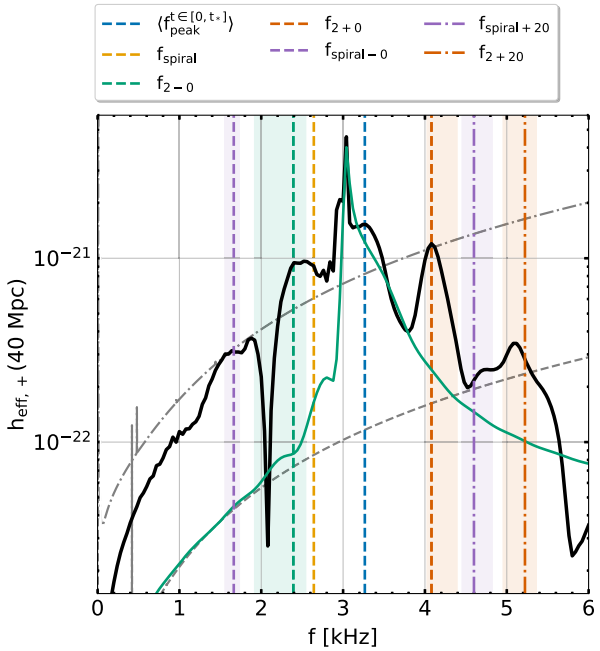

FIG. 22. Effective GW spectra $h_{\mathrm{eff},+}(f)$ for simulation and simplified analytic model for $M_{\mathrm{tot}} = 3.1\ M_{\odot}$ model. The black line corresponds to the simulation. The green line displays the simplified one-component analytic model (A1). Dashed and dash-dotted vertical lines indicate secondary frequencies $\langle f_{\mathrm{peak}}^{t\in[0,t_*]}\rangle$, f_{spiral}, $f_{2\pm0}$, $f_{\mathrm{spiral}-0}$, f_{2+20}, and $f_{\mathrm{spiral}+20}$. Shaded areas visualize their respective spread due to the time-evolving frequencies.

The blue curve in Fig. 21 includes the $f_{\mathrm{spiral}-0}$ component, whose frequency we assume to be constant and we also adopt constant values for $f_{2\pm0}$ as in the original model. We do not incorporate an $f_{\mathrm{spiral}+0}$ component in our modified analytic model since we do not observe a distinct peak in the GW spectrum at the respective frequency. The parameters $A_{\mathrm{spiral}-0}$ and $\tau_{\mathrm{spiral}-0}$ are derived from the spectrograms as described in Sec. V C 3.

The inclusion of the $f_{\mathrm{spiral}-0}$ component substantially increases the fitting factor $\mathrm{FF}_{\mathrm{new},2} = 0.962$. This leads to a significant improvement regarding the reduction in the detection rates of 11%. The importance of the $f_{\mathrm{spiral}-0}$ component is also apparent in the GW spectrum (compare orange and blue curve below 2 kHz). As previously mentioned, the strength of $f_{\mathrm{spiral}-0}$ relative to the frequency-dependent sensitivity curve is similar to f_{2+0} (for this mass configuration) and thus has a large impact on the FF.

We remark that the first modification [time-evolving $f_{2\pm0}(t)$] only slightly improves the analytic fits but increases the complexity of the model since a parametrization of $f_{2\pm0}(t)$ would require a number of additional parameters. The second modification (inclusion of $f_{\mathrm{spiral}-0}$) improves significantly the analytic fits (FFs) and only introduces a minimum of new parameters ($A_{\mathrm{spiral}-0}$, $\tau_{\mathrm{spiral}-0}$, and $\phi_{\mathrm{spiral}-0}$, while the frequency is already given by the other components).

B. Additional spectral features

We finally note that the different components and their couplings provide explanations for basically every feature in the GW spectrum up to about 6 kHz if one additionally considers higher-order combination tones. This is shown in Fig. 22, where we in addition draw the fit for the simplified analytic model (green curve). We estimate those additional frequencies employing the dominant frequency at early times $\langle f_{\mathrm{peak}}^{t\in[0,t_*]}\rangle$ and using expressions $f_{2+20} \approx \langle f_{\mathrm{peak}}^{t\in[0,t_*]}\rangle + 2\cdot f_0$ and $f_{\mathrm{spiral}+20} \approx f_{\mathrm{spiral}} + 2\cdot f_0$. We derive the respective frequency ranges inserting the time evolution of $f_0(t)$ and $f_{\mathrm{peak}}^{\mathrm{analytic}}(t)$. The estimated frequency ranges for f_{2+20} and $f_{\mathrm{spiral}+20}$ match relatively well with peaks in the GW spectrum. We note that the frequencies f_{2+20} and $f_{\mathrm{spiral}+20}$ are also expected to follow empirical relations, which can be exploited in more sophisticated analytic models.

Finally, we remark that the frequency component f_{2-20} is most likely less important than $f_{\mathrm{spiral}-0}$. Our estimation using the expression $f_{2-20} \approx \langle f_{\mathrm{peak}}^{t\in[0,t_*]}\rangle - 2\cdot f_0$ leads to $f_{2-20} = 1.309$ kHz, which is significantly lower than the peak in the GW spectrum ($f_{\mathrm{spiral}-0} = 1.664$ kHz).

Another relevant feature is the reexcitation of the quadrupolar mode f_{peak}, which occurs roughly 10 ms after

merging in high-mass models (see Appendix C 2) possibly due to the excitation of a low-$|T/W|$ rotational instability (see e.g., [117–119] and references therein). This feature is not captured by the adopted single exponential decay of the amplitude.

IX. CONCLUSIONS

In this work, we investigate the spectral properties of the GW emission for a mass sequence of binary neutron star mergers and introduce an analytic model for the postmerger GW emission, which employs exponentially decaying sinusoids. We discuss the features of the GW spectra and their dependence on total binary mass. We also study the time evolution of certain frequency components using spectrograms. Notably, we find that the $f_{\rm peak}$ mode exhibits a time evolution which can be split in two phases: (a) a rapid initial drift and (b) an approximately constant frequency at late times. We identify a new mechanism which explains a low-frequency peak (in the GW spectra) occurring in high-mass configurations. It is caused by a coupling between the antipodal bulges ($f_{\rm spiral}$) and the quasiradial mode (f_0). Our analytic model incorporates a time-dependent $f_{\rm peak}(t)$ and three secondary components ($f_{\rm spiral}$ and $f_{2\pm0}$). We evaluate the model's performance using the noise-weighted FF and find good agreement with the simulations with FF > 0.95 for the majority of the models. We explore the dependencies of the analytic model's parameters, and correlations among them, on the total mass $M_{\rm tot}$. Finally, we include potential modifications to the analytic model for the configurations with $M_{\rm tot}$ close to $M_{\rm thres}$.

All models of the mass sequence exhibit a time-dependent $f_{\rm peak}(t)$. In their GW spectra, $f_{\rm peak}$ is one-sided toward high frequencies. We model this evolution with a two-segment piecewise function Eq. (1) and quantify the drift using spectrograms of the simulation signals. The analytic model reproduces remarkably well the one-sided $f_{\rm peak}$ structure and thus it confirms that our choice is sufficient for the description of such time-dependent $f_{\rm peak}(t)$. We note that $\langle f_{\rm peak}^{t\in[0,t_*}\rangle$ is a good measure of $f_{\rm peak}$ in the early postmerger phase. We find that the parameters characterizing the time evolution of $f_{\rm peak}(t)$ ($\zeta_{\rm drift}$, t_*, and $f_{\rm peak,0}$) show a dependence on total mass $M_{\rm tot}$. The frequency evolution becomes faster for high-mass configurations. We note that such trends may provide information on the proximity to prompt collapse.

We confirm that the postmerger GW spectra follow the classification scheme introduced in [37]. As the total mass $M_{\rm tot}$ increases and the quasiradial mode is stronger excited, the secondary components $f_{2\pm0}$ become more pronounced and there is an overlap between f_{2-0} and $f_{\rm spiral}$. In low-mass configurations a low-frequency modulation $f_{\rm peak} - f_{\rm spiral}$ is seen in $\alpha_{\rm min}(t)$ with comparable strength to that of the quasiradial mode.

Using the analytic model's parameters, amplitudes and decay timescales A_i and τ_i, we find that the products $(A\cdot\tau)_i$ for the mass sequence can be used to quantitatively define the strength of secondary components (for $i = {\rm spiral}, 2\pm0$) and allow a *quantitative classification* of the different types of spectra as in [37].

Furthermore, we identify a new mechanism generating a potentially relevant secondary GW feature: In high-mass configurations the coupling between $f_{\rm spiral}$ and f_0 leads to frequencies at approximately $f_{\rm spiral\pm0} \approx f_{\rm spiral} \pm f_0$. We note that relative to the sensitivity curve, $f_{\rm spiral-0}$ is comparable to f_{2+0}.

We hypothesize couplings to the overtones of the quasiradial mode, such as f_{2+20} and $f_{\rm spiral+20}$, and identify frequency peaks in the GW spectrum near their vicinity such that we explain nearly all visible frequency peaks.

The analytic model leads to FFs (assuming the sensitivity curve of ET) in the range of [0.907–0.979] where the majority of the models have FF > 0.95 and only the $M_{\rm tot} = 3.1\ M_\odot$ configuration (close to $M_{\rm thres}$) has FF $= 0.907$. We find that for this configuration the inclusion of the $f_{\rm spiral-0}$ component significantly increases the fitting factor to FF $= 0.962$. We further assessed our analytic model by considering simplified analytic models with fewer frequency components. We find that postmerger GW templates should incorporate at least two secondary components such as $f_{\rm spiral}$ and f_{2-0}. The simplified model with one secondary component leads to a large reduction in detection rates. Using an additional simplified analytic model which incorporates a constant $f_{\rm peak}$ and three secondary components, we find that an accurate description of $f_{\rm peak}(t)$ is crucial for obtaining higher FFs, at least for the particular EOS studied here.

We find systematic dependencies for all the analytic model's parameters with respect to the total binary mass $M_{\rm tot}$. A_i and τ_i (for $i = {\rm peak}, {\rm spiral}, 2\pm0$) correlate with $M_{\rm tot}$ and follow trends which we model using second-order polynomials. Some of these trends, such as A_{2-0} and $\tau_{\rm spiral}$, are not particularly tight but the dependence on mass is clear. We also find tight correlations between the initial phases ϕ_i (for $i = {\rm peak}, {\rm spiral}, 2\pm0$) of each component with the total mass $M_{\rm tot}$ and between the secondary component initial phases $\phi_{\rm spiral}$, $\phi_{2\pm0}$ and $\phi_{\rm peak}$ which may suggest a constant phase difference between the $f_{\rm peak}$ and secondary components.

One possible limitation of our analytic model is that it includes a relatively large number of parameters, which results from the complexity of the problem. However, all of them show a clear dependence on the total binary mass $M_{\rm tot}$ and can be modeled by analytic relations. These can potentially be used to decrease the parameter space in

data analysis techniques. Furthermore, we note that the tight relations between the initial phases $\phi_{\rm peak}$ and $\phi_{\rm spiral}$, $\phi_{2\pm0}$ should be further explored.

In our analysis, we applied a hierarchical procedure to initially estimate a subset of the analytic model's parameters and to then determine the remaining parameters using a curve fitting procedure (trust-region-reflective algorithm). Ideally, one would employ more sophisticated parameter estimation techniques, which provide distributions in the parameter space.

In future work, we plan to evaluate the model's performance for a large sample of EOSs and for unequal-mass mergers.

ACKNOWLEDGMENTS

T. S. thanks Georgios Lioutas for the useful discussions. The work of T. S. is supported by the Klaus Tschira Foundation. T. S. is supported by a fellowship of the International Max Planck Research School for Astronomy and Cosmic Physics at the University of Heidelberg (IMPRS-HD) and acknowledges financial support from IMPRS-HD. T. S. acknowledges support by the High Performance and Cloud Computing Group at the Zentrum für Datenverarbeitung of the University of Tübingen, the state of Baden-Württemberg through bwHPC and the German Research Foundation (DFG) through Grant No. INST 37/935-1 FUGG. A. B. acknowledges support by the European Research Council (ERC) under the European Unions Horizon 2020 research and innovation program under Grant Agreement No. 759253, support by Deutsche Forschungsgemeinschaft (DFG, German Research Foundation)—Project-ID 279384907—SFB 1245 and DFG—Project-ID 138713538—SFB 881 (The Milky Way System, subproject A10), and support by the State of Hesse within the Cluster Project ELEMENTS. N. S. gratefully acknowledges the Italian Istituto Nazionale di Fisica Nucleare (INFN), the French Centre National de la Recherche Scientifique (CNRS) and the Netherlands Organization for Scientific Research, for the construction and operation of the Virgo detector and the creation and support of the EGO consortium. Computing time was provided, in part, by allocations on the ARIS supercomputing facility of GRNET in Athens (SIMGRAV, SIMDIFF and BNSMERGE allocations) and by the Aristoteles Cluster at AUTh.

APPENDIX A: NUMERICAL SETUP

In this section we further discuss our numerical setup. We address the impact of residual eccentricity in the ID, of the initial orbital separation, of the numerical resolution, and of pi symmetry on the spectral features.

1. Effect of residual eccentricity in ID and of initial orbital separation

In this section we address the effect of the residual eccentricity in the ID to the spectral features. To minimize the initial eccentricity in the ID we implement the prescription introduced in [120] and adapt it to the field equations solved within LORENE [77].

We carry out two additional simulations with total binary mass $M_{\rm tot} = 2.5\ M_\odot$ (as in the reference simulation) and initial separation distance of $d = 50$ km. The reduction of eccentricity is achieved with an iterative procedure (described in [120]), which uses a few revolutions during the inspiral. It performs better at large initial separation, e.g., $d = 50$ km, which is why we choose a larger d for these tests. Otherwise the numerical setup is the same as for the mass sequence simulations (see Sec. II). Considering these two additional simulations we can assess the impact of eccentricity on the spectral features since this is the only parameter, which differs between those two calculations. We refer to the simulation with the quasicircular ID and the simulation with reduced eccentricity as QC and RE, respectively.

In order to compute the separation distance between the two NSs, we assume that the center of mass of the star coincides with the location of the maximum rest-mass density $\rho_{\rm max}$. We use these coordinates $(x_{\rm max}, y_{\rm max})$ in the orbital plane and define the separation distance by

$$d(t) = 2 \cdot \sqrt{x_{\rm max}^2 + y_{\rm max}^2}, \tag{A1}$$

where the factor 2 reflects the pi symmetry of the system.

Figure 23 shows the time evolution of the coordinate separation distance $d(t)$ for both simulations. We estimate the eccentricity using the method described in [120]. The residual eccentricity in the QC simulation is $e \approx 0.0088$ and the reduced residual eccentricity of the RE simulation is

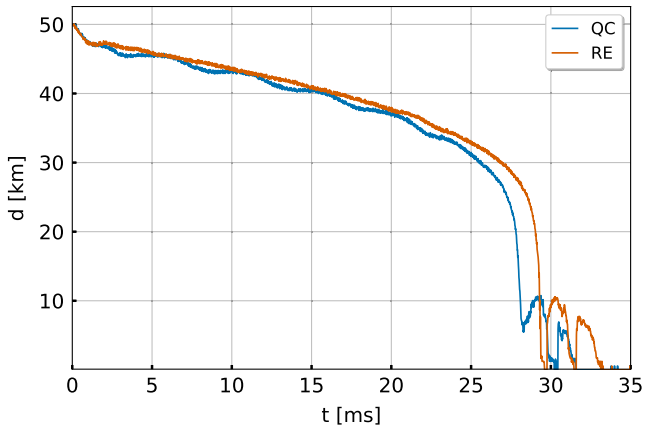

FIG. 23. Time evolution of the coordinate separation distance $d(t)$ for the simulations QC (blue) and RE (orange).

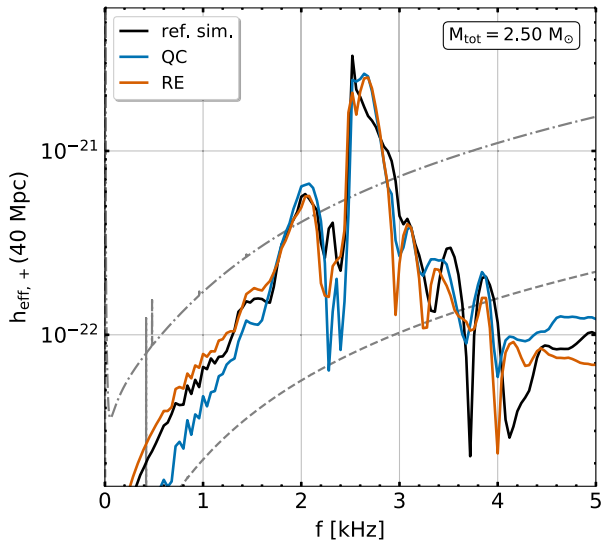

FIG. 24. Effective GW spectra $h_{\mathrm{eff},+}(f)$ for the reference simulation (black) and simulations QC (blue) and RE (orange). The dash-dotted curves denote the design sensitivity Advanced LIGO [108] and of the Einstein Telescope [109], respectively.

$e \approx 0.00089$. The QC simulation exhibits small modulations in the separation distance $d(t)$, while in the RE simulation these oscillations disappear, as expected due to the reduced eccentricity.

Figure 24 displays the GW spectra for the reference simulation and the simulations QC and RE. The spectra agree in the general features and their morphology, and the frequency peaks coincide. They exhibit an f_{peak} which is one-sided and a dominant secondary peak, f_{spiral}, with comparable strength. Therefore it is unlikely that the residual eccentricity in the ID affects the mechanisms for the frequency of evolution of f_{peak} or the formation of the antipodal bulges and thus f_{spiral}. There are small differences in the amplitudes of the frequency peaks, which might be explained by differences in the impact velocities during the collision. However, these differences can also be seen between the reference simulation and the simulation QC, which only differ in initial separation distance. In particular, the morphology of the main peak is to some extent affected by the initial orbital separation.

We compute the analytic (Ac) and semianalytic (Sc) model fits for the two simulations and find large fittings factors of FF $\gtrsim 0.970$ (see Table VI). We overplot the initial

TABLE VI. FFs for the analytic (Ac) and semianalytic (Sc) model fits for the simulations QC and RE.

	FFs	
Simulation	Sc	Ac
QC	0.969	0.978
RE	0.981	0.979

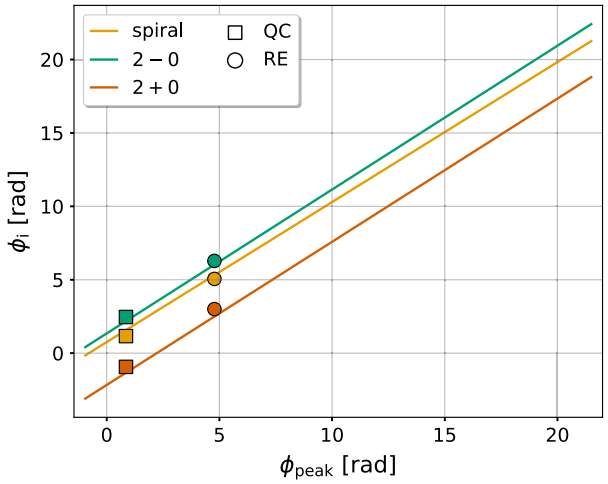

FIG. 25. Initial phases ϕ_i (for $i =$ spiral, 2 ± 0) with respect to ϕ_{peak} for the analytic model (Ac) fits for the simulations QC (square) and RE (circle). Colored lines correspond to Eqs. (22)–(24).

phases ϕ_i (for $i =$ peak, spiral, 2 ± 0) together with Eqs. (22)–(24) in Fig. 25. We find that the tight correlations between the phases still hold and the impact of residual eccentricities is negligible. We note that the initial phases ϕ_i (for $i =$ peak, spiral, 2 ± 0) are shifted with additions or subtractions of multiples of 2π.

2. Resolution study

In this section we discuss the impact of resolution on the spectral properties. We consider an additional high-resolution simulation with total binary mass $M_{\mathrm{tot}} = 2.5\ M_\odot$ (as in the reference model) and finest grid spacing of $dx =$ 185 m (keeping the same number of refinement levels). Apart from the resolution, the numerical setup is identical to the one described in Sec. II. We refer to the high-resolution simulation as HR.

Figure 26 displays the GW spectra for the reference and HR simulation. The agreement between the frequency peaks is remarkable, although there are small differences in the morphology of the main peak. The time evolution of $f_{\mathrm{peak}}(t)$ agrees well in both simulations, and we observe a very good agreement between the secondary frequencies, especially for f_{spiral} and f_{2-0}. Figure 27 shows the spectrograms for the two simulations and confirms that, in spite of the differences in the structure of the main peak shown in the spectra of Fig. 26, the time evolution of $f_{\mathrm{peak}}(t)$ is qualitatively similar in both cases and it can thus be described by the same analytic model that we describe in the main text.

We also compute the analytic (Ac) and semianalytic (Sc) model fits for the HR simulation and find large fitting factors of FF $\gtrsim 0.970$ (see Table VII). We note that for this particular configuration the FFs are even larger than the ones obtained for the reference simulation.

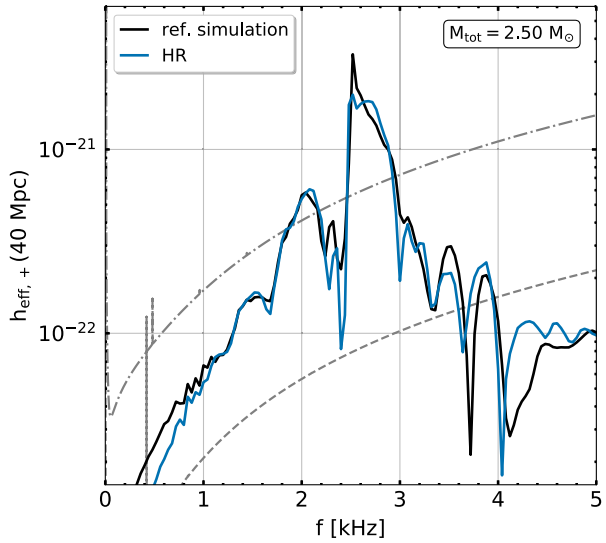

FIG. 26. Effective GW spectra $h_{\mathrm{eff},+}(f)$ for the reference simulation (black) and the high-resolution simulation HR (blue). The dash-dotted curves denote the design sensitivity Advanced LIGO [108] and of the Einstein Telescope [109], respectively.

TABLE VII. FFs for the analytic (Ac) and semianalytic (Sc) model fits for the HR simulation.

	FFs	
Simulation	Sc	Ac
Ref.	0.969	0.956
HR	0.978	0.974

3. Effect of pi symmetry

In this section we discuss the impact of imposing pi symmetry during the simulations. We carry out additional simulations using the same numerical setup as described in Sec. II but without pi symmetry. We run additional models for $M_{\mathrm{tot}} = 2.5\ M_\odot, 2.7\ M_\odot, 2.9\ M_\odot$ and $3.0\ M_\odot$. The respective spectra agree very well with the simulations using pi symmetry. As example, we show the calculation for $M_{\mathrm{tot}} = 3.0\ M_\odot$ in Fig. 28. This particular configuration is discussed in Sec. III C. We conclude that imposing pi symmetry does not impact the spectral features and in particular the $f_{\mathrm{spiral}\pm 0}$ coupling is unaffected by the pi symmetry.

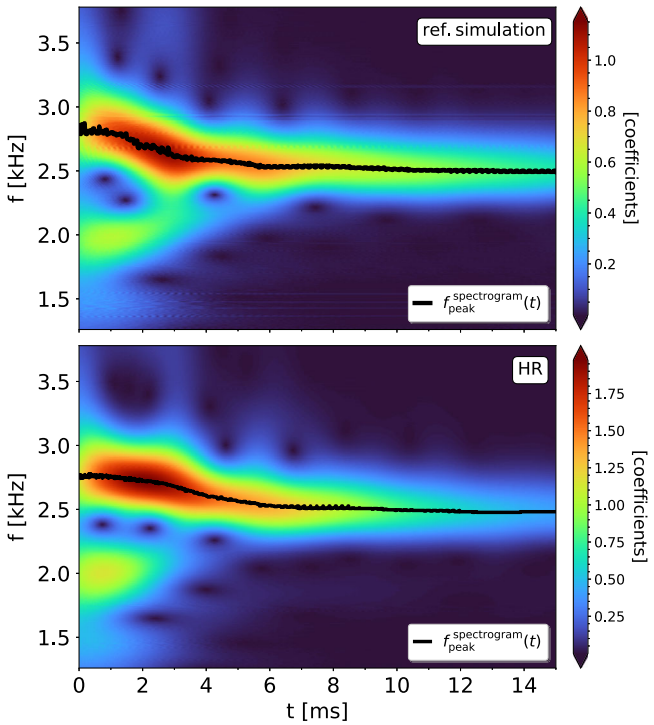

FIG. 27. Top panel: spectrogram of $h_+(t)$ for the reference simulation. Bottom panel: spectrogram of $h_+(t)$ for the high-resolution simulation HR. The black curves correspond to the numerically extracted $f^{\mathrm{spectrogram}}_{\mathrm{peak}}(t)$ for the reference simulation and HR, respectively.

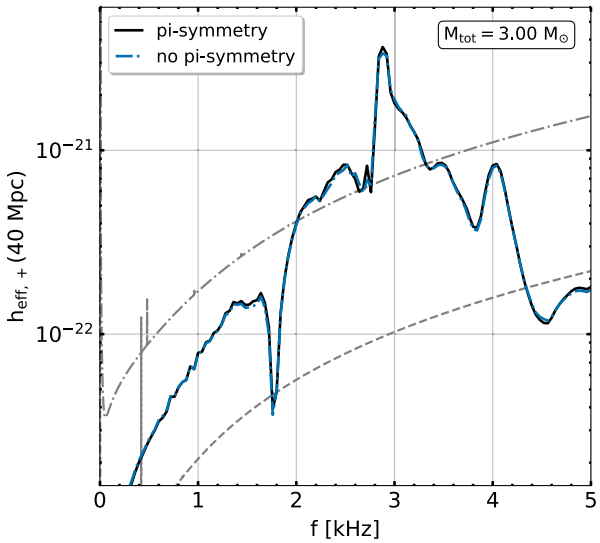

FIG. 28. Effective GW spectra $h_{\mathrm{eff},+}(f)$ for the $M_{\mathrm{tot}} = 3.0\ M_\odot$ simulation with pi symmetry (black) and without pi symmetry (blue). The dash-dotted curves denote the design sensitivity Advanced LIGO [108] and of the Einstein Telescope [109], respectively.

APPENDIX B: SPECTRAL PROPERTIES OF THE MASS SEQUENCE MODELS

We present supplementary figures for the mass sequence models. Figure 29 shows the GW spectra including the inspiral signal. Figure 30 displays the spectrograms for the postmerger GW signal $h_+(t)$. Figure 31 provides the spectrograms for the minimum lapse function $\alpha_{\min}(t)$ starting at a few milliseconds before the merging phase.

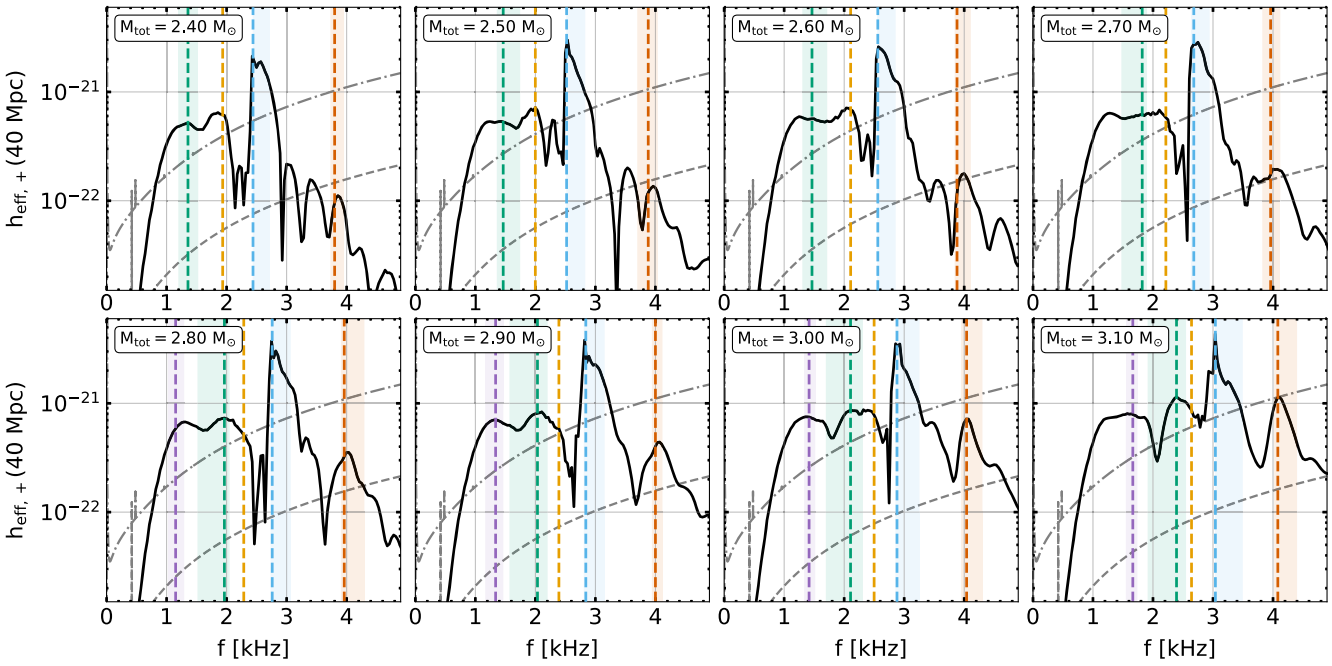

FIG. 29. As in Fig. 2 but including the inspiral signal.

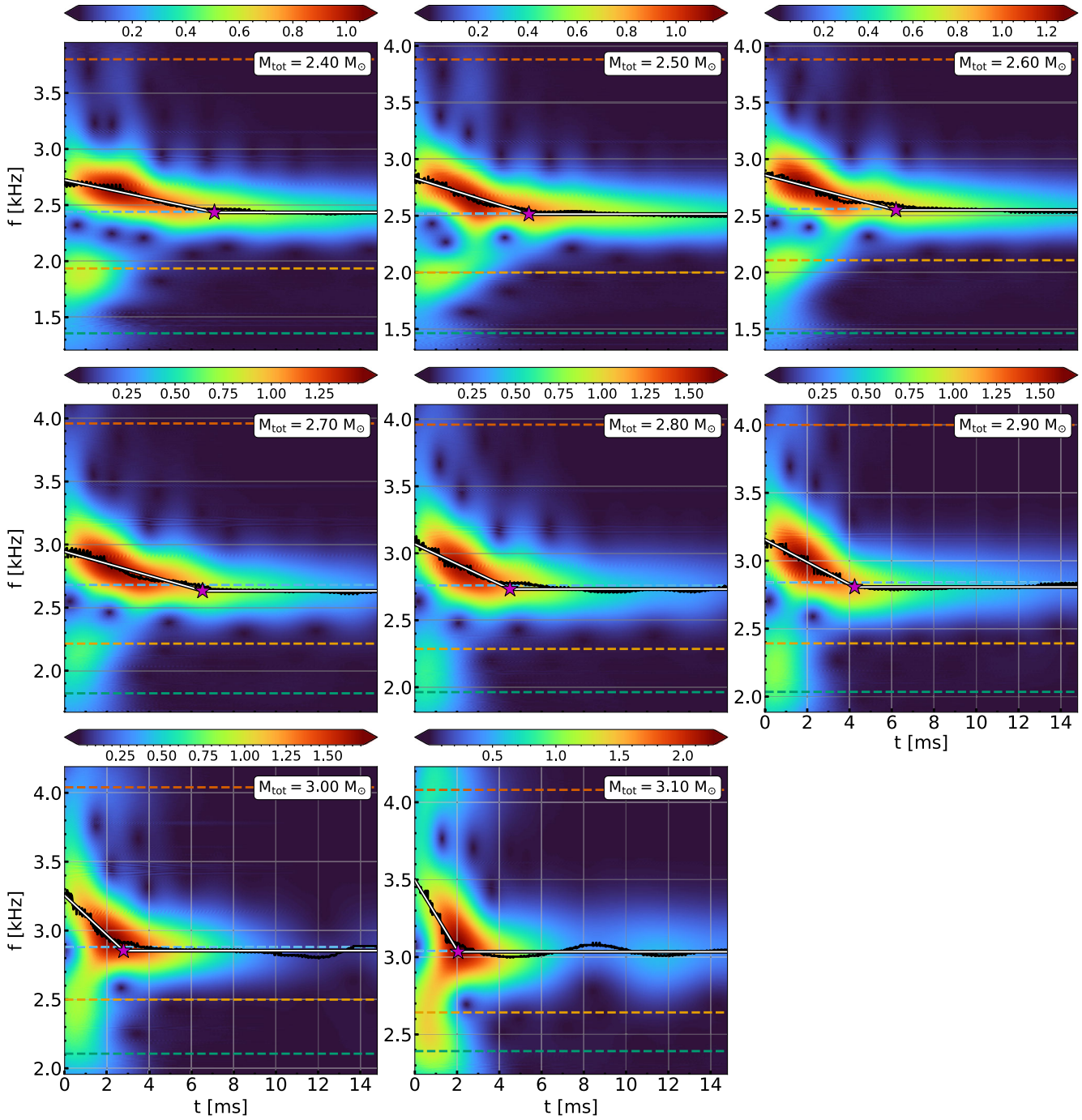

FIG. 30. As in Fig. 1 but for all models in our mass sequence.

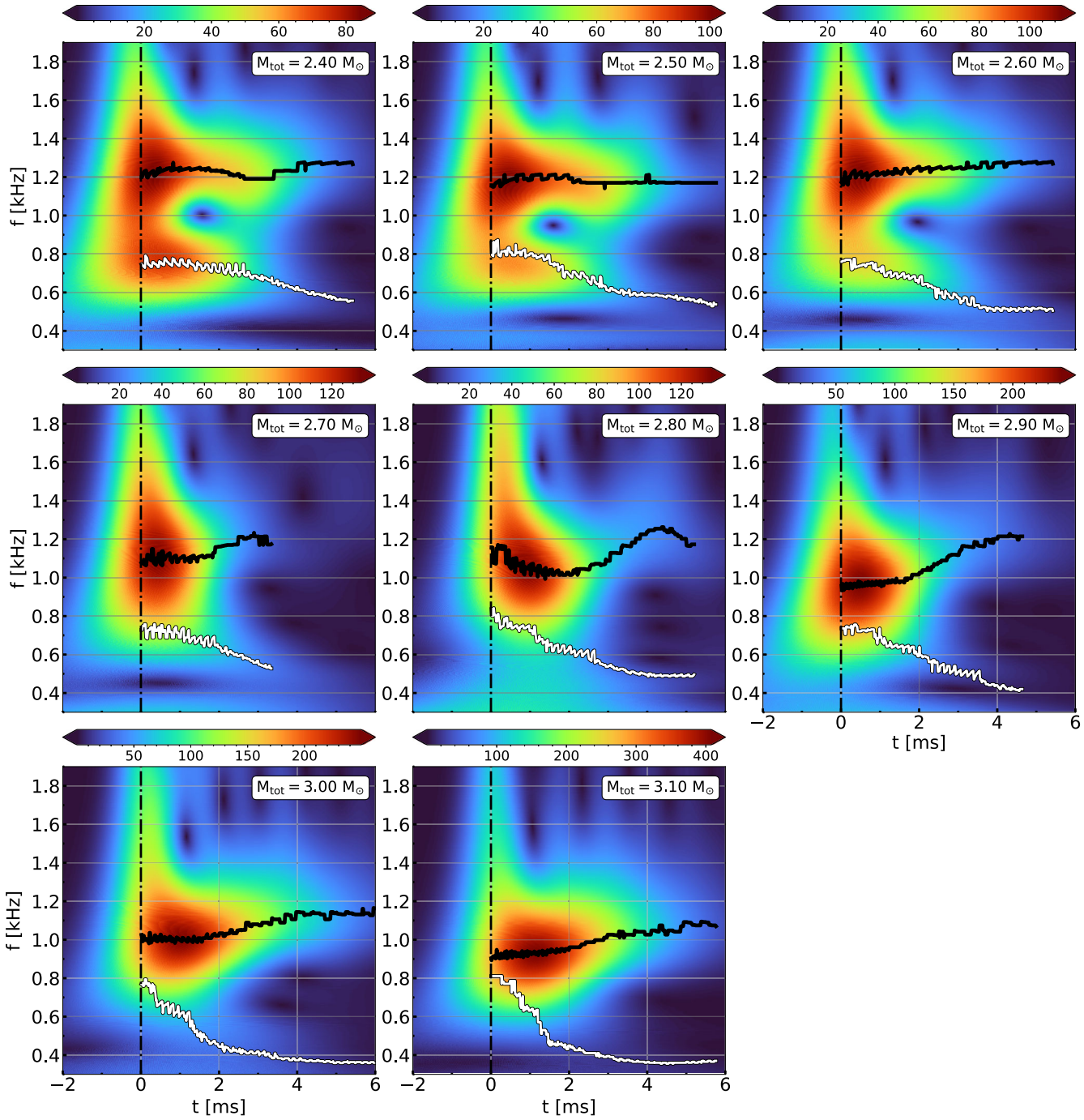

FIG. 31. As in Fig. 3 but for all models of our mass sequence.

APPENDIX C: ANALYTIC MODEL

1. Spectrogram analysis

To further evaluate the analytic model, we quantitatively analyze the spectrograms of the numerical simulation and of the analytic fit. Figures 32(a)–32(c) depict the wavelet coefficients $\mathcal{A}_{\mathrm{peak}}(t)$, $\mathcal{A}_{\mathrm{spiral}}(t)$, and $\mathcal{A}_{2-0}(t)$, which we extract at the corresponding frequencies from the spectrograms as function of time, for the simulation (blue line) and for the analytic fit (orange line). The analytic model performs well in reproducing the three coefficients of the simulation data. For illustration purposes, we omit the

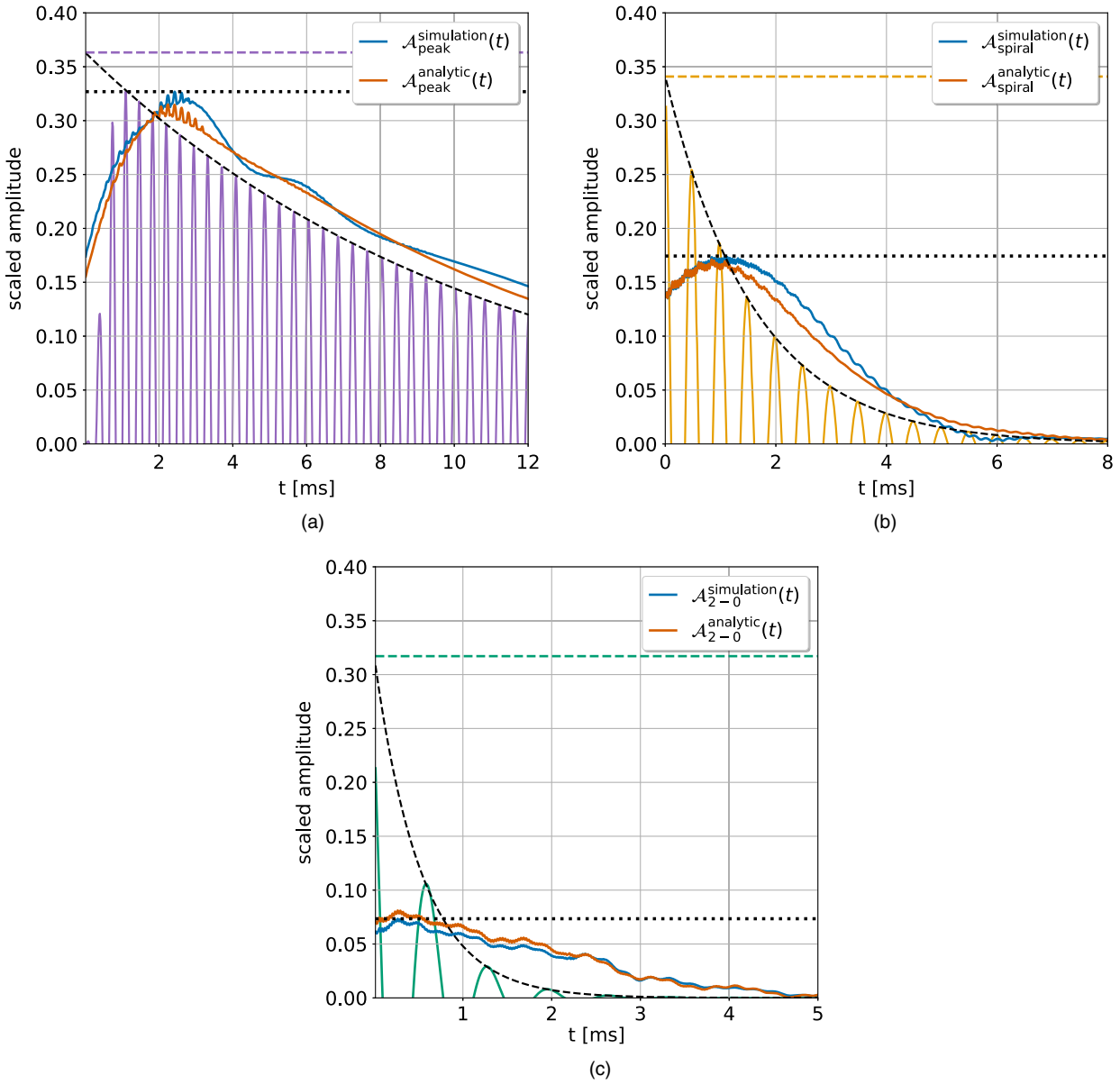

FIG. 32. Top left panel: coefficient curves $\mathcal{A}_{\mathrm{peak}}(t)$ for the f_{peak} component extracted from the spectrograms of simulation and analytic model. The purple dashed line indicates amplitude A_{peak}. The black dotted horizontal line shows the maximum of $\mathcal{A}_{\mathrm{peak}}(t)$ for simulation. The purple sinusoidal function shows f_{peak} component as used in the analytic model. The dashed black curve shows its exponential decay. Top right panel: coefficient curves $\mathcal{A}_{\mathrm{spiral}}(t)$ for the f_{spiral} component extracted from spectrograms of simulation and analytic model. The yellow dashed line shows the amplitude A_{spiral}. The black dotted horizontal line indicates the maximum of $\mathcal{A}_{\mathrm{spiral}}(t)$ for simulation. The yellow sinusoidal function shows f_{spiral} component as used in the analytic model. The dashed black curve shows its exponential decay. Bottom panel: coefficient curves $\mathcal{A}_{2-0}(t)$ for the f_{2-0} component extracted from spectrograms of simulation and analytic model. The yellow dashed line shows amplitude A_{2-0}. The black dotted horizontal line indicates the maximum of $\mathcal{A}_{2-0}(t)$ for simulation. The yellow sinusoidal function shows the f_{2-0} component as used in the analytic model. The dashed black curve shows its exponential decay.

normalization factor $\mathcal{N}$ and overlay the corresponding exponentially decaying sinusoid functions for each frequency component while we rescale the coefficient curves by a constant factor which ensures that the maxima of $(h_{\rm peak}(t)\mathcal{W}(t;s))$ and $\mathcal{A}_{\rm peak}(t)$ coincide.

We note that the three components exhibit different magnitudes of the coefficient curves $\mathcal{A}_i(t)$, whereas the amplitudes A_i $(i = \text{peak}, \text{spiral}, 2-0)$ of the analytic model are roughly comparable. For our reference simulation with a total binary mass $M_{\rm tot} = 2.5\ M_\odot$, we actually expect that the $f_{\rm spiral}$ component is the strongest secondary feature, which is also suggested by the GW spectrum, and in fact the maxima of the coefficients show this hierarchy. We thus remark that the amplitudes A_i of the analytic model may have only a limited physical meaning, while other quantities, such as the surface area under $\mathcal{A}_i(t)$, the maxima of $\mathcal{A}_i(t)$ or the product $A_i \cdot \tau_i$ may turn out to be more representative for the merger dynamics and GW emission.

2. Sequence of simulations with different masses

Figure 33 shows the time-domain signals for the simulation and the analytic model along the sequence of simulations with different masses. Notice the possible excitation of a low-$|T/W|$ rotational instability in the highest-mass model, after $\sim$10 ms from the onset of merger [117–119].

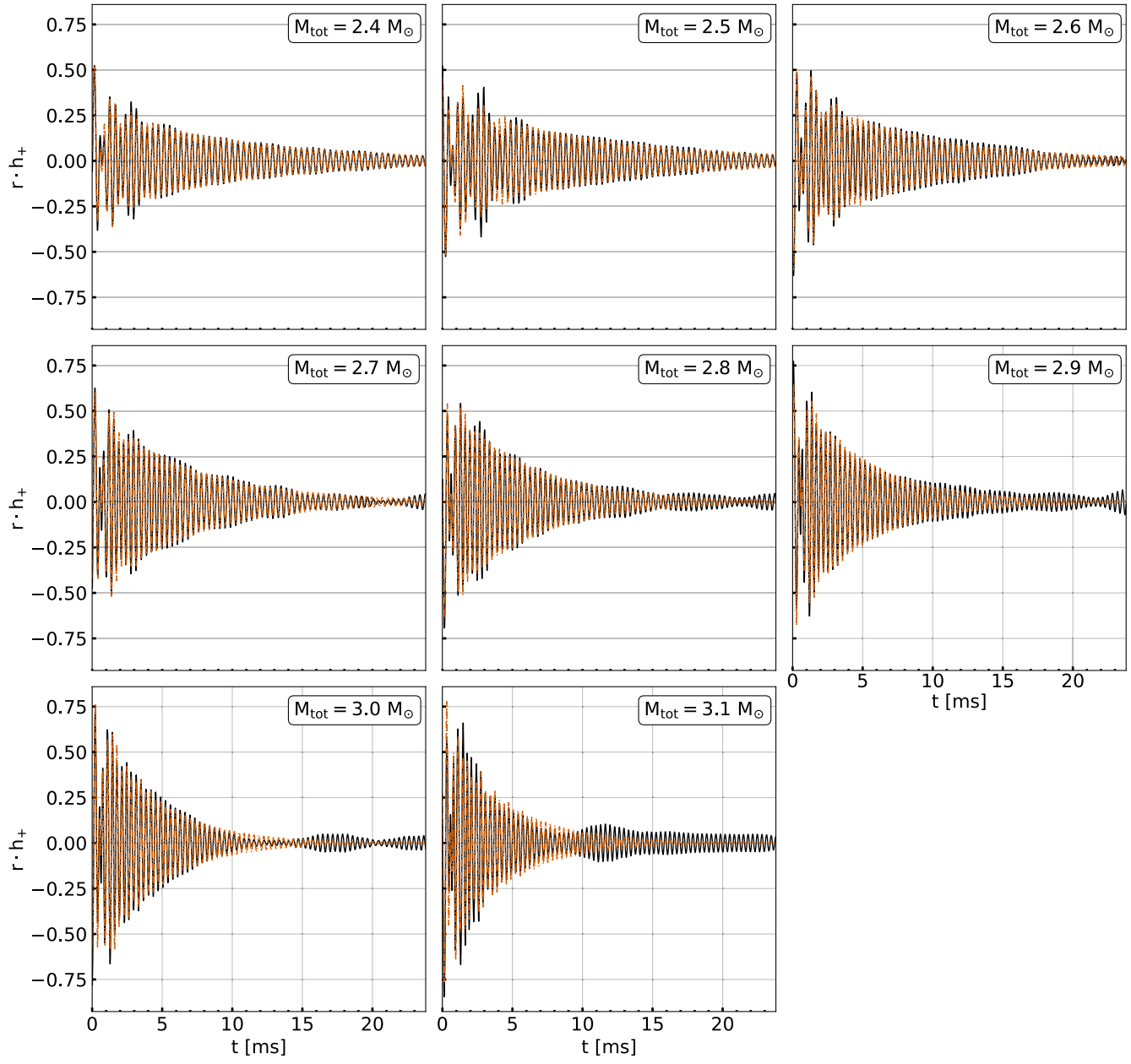

FIG. 33. As in Fig. 8 but for all models of our mass sequence.

3. Initial phases

We find that the initial phases $\phi_{\rm peak}$, $\phi_{\rm spiral}$, and $\phi_{2\pm0}$ correlate with the total binary mass $M_{\rm tot}$. We model this dependence with a two-segment piecewise function consisting of two linear fits which intersect at $M_{\rm tot} = 2.7\ M_\odot$. These are given by

$$\phi_{\rm peak} = \begin{cases} +18.957 \cdot M_{\rm tot} - 46.321 & \text{for } M_{\rm tot} \leq 2.7\ M_\odot, \\ +43.425 \cdot M_{\rm tot} - 113.152 & \text{for } M_{\rm tot} > 2.7\ M_\odot, \end{cases} \tag{C1}$$

$$\phi_{\rm spiral} = \begin{cases} +17.580 \cdot M_{\rm tot} - 42.199 & \text{for } M_{\rm tot} \leq 2.7\ M_\odot, \\ +40.448 \cdot M_{\rm tot} - 104.258 & \text{for } M_{\rm tot} > 2.7\ M_\odot, \end{cases} \tag{C2}$$

$$\phi_{2-0} = \begin{cases} +18.541 \cdot M_{\rm tot} - 43.911 & \text{for } M_{\rm tot} \leq 2.7\ M_\odot, \\ +43.613 \cdot M_{\rm tot} - 112.705 & \text{for } M_{\rm tot} > 2.7\ M_\odot, \end{cases} \tag{C3}$$

$$\phi_{2+0} = \begin{cases} +16.064 \cdot M_{\rm tot} - 41.163 & \text{for } M_{\rm tot} \leq 2.7\ M_\odot, \\ +43.309 \cdot M_{\rm tot} - 115.341 & \text{for } M_{\rm tot} > 2.7\ M_\odot. \end{cases} \tag{C4}$$

4. Empirical relations

The fits are carried out for the signals $r \cdot h_s(t)$ (for $s = +, \times$). Table VIII provides information about the analytic model's parameters.

TABLE VIII. The analytic model's parameters.

Analytic model's parameters		
Symbol	Unit	Equation
M	$M_\odot$	⋯
$h_{\rm eff,+}(f) = f \cdot \tilde{h}_+(f)$	Dimensionless	⋯
Sensitivity curve $\equiv\sqrt{S_h(f) \cdot f}$	Dimensionless	⋯
$f_{\rm peak}$	kHz	⋯
$f_{\rm spiral}$	kHz	⋯
$f_{2\pm0}$	kHz	⋯
$f_{\rm spiral\pm0}$	kHz	⋯
$\zeta_{\rm drift}$	kHz^2	(10)
$f_{\rm peak,0}$	kHz	(11)
t_*	ms	(12)
$A_{\rm peak}$	Dimensionless	(13)
$\tau_{\rm peak}$	ms	(14)
$\tau_{\rm spiral}$	ms	(15)
τ_{2-0}	ms	(16)
τ_{2+0}	ms	(17)
$A_{\rm spiral}$	Dimensionless	(18)
A_{2-0}	Dimensionless	(19)
A_{2+0}	Dimensionless	(20)
$\mathcal{N}$	Dimensionless	(21)
$\phi_{\rm peak}$	rad	(C1)
$\phi_{\rm spiral}$	rad	(22), (C2)
ϕ_{2-0}	rad	(23), (C3)
ϕ_{2+0}	rad	(24), (C4)

[1] B. P. Abbott, R. Abbott, T. D. Abbott, F. Acernese, K. Ackley, C. Adams, T. Adams, P. Addesso, R. X. Adhikari, V. B. Adya *et al.* (LIGO Scientific Collaboration and Virgo Collaboration), GW170817: Observation of Gravitational Waves from a Binary Neutron Star Inspiral, Phys. Rev. Lett. **119**, 161101 (2017).

[2] B. P. Abbott, R. Abbott, T. D. Abbott, S. Abraham, F. Acernese, K. Ackley, C. Adams, R. X. Adhikari, V. B. Adya, C. Affeldt *et al.*, GW190425: Observation of a compact binary coalescence with total mass ~3.4 $M_\odot$, Astrophys. J. Lett. **892**, L3 (2020).

[3] B. P. Abbott *et al.* (KAGRA, LIGO Scientific, VIRGO Collaborations), Prospects for observing and localizing gravitational-wave transients with Advanced LIGO, Advanced Virgo and KAGRA, Living Rev. Relativity **21**, 3 (2018).

[4] B. P. Abbott *et al.* (LIGO Scientific and Virgo Collaborations), Properties of the Binary Neutron Star Merger GW170817, Phys. Rev. X **9**, 011001 (2019).

[5] K. Chatziioannou, Neutron-star tidal deformability and equation-of-state constraints, Gen. Relativ. Gravit. **52**, 109 (2020).

[6] T. Dietrich, T. Hinderer, and A. Samajdar, Interpreting binary neutron star mergers: Describing the binary neutron star dynamics, modelling gravitational waveforms, and analyzing detections, Gen. Relativ. Gravit. **53**, 27 (2021).

[7] A. Bauswein, O. Just, H.-T. Janka, and N. Stergioulas, Neutron-star radius constraints from GW170817 and future detections, Astrophys. J. Lett. **850**, L34 (2017).

[8] B. P. Abbott *et al.* (LIGO Scientific and Virgo Collaborations), GW170817: Measurements of Neutron Star Radii and Equation of State, Phys. Rev. Lett. **121**, 161101 (2018).

[9] D. Radice and L. Dai, Multimessenger parameter estimation of gw170817, Eur. Phys. J. A **55**, 50 (2019).

[10] C. D. Capano, I. Tews, S. M. Brown, B. Margalit, S. De, S. Kumar, D. A. Brown, B. Krishnan, and S. Reddy, Stringent constraints on neutron-star radii from multimessenger

observations and nuclear theory, Nat. Astron. **4**, 625 (2020).
[11] T. Dietrich, M. W. Coughlin, P. T. H. Pang, M. Bulla, J. Heinzel, L. Issa, I. Tews, and S. Antier, Multimessenger constraints on the neutron-star equation of state and the Hubble constant, Science **370**, 1450 (2020).
[12] P. Landry, R. Essick, and K. Chatziioannou, Nonparametric constraints on neutron star matter with existing and upcoming gravitational wave and pulsar observations, Phys. Rev. D **101**, 123007 (2020).
[13] M. Breschi, A. Perego, S. Bernuzzi, W. Del Pozzo, V. Nedora, D. Radice, and D. Vescovi, AT2017GFO: Bayesian inference and model selection of multi-component kilonovae and constraints on the neutron star equation of state, Mon. Not. R. Astron. Soc. **505**, 1661 (2021).
[14] G. Raaijmakers, S. K. Greif, K. Hebeler, T. Hinderer, S. Nissanke, A. Schwenk, T. E. Riley, A. L. Watts, J. M. Lattimer, and W. C. G. Ho, Constraints on the dense matter equation of state and neutron star properties from NICER's mass-radius estimate of PSR J0740 + 6620 and multimessenger observations, Astrophys. J. Lett. **918**, L29 (2021).
[15] I. Legred, K. Chatziioannou, R. Essick, S. Han, and P. Landry, Impact of the PSR J 0740 + 6620 radius constraint on the properties of high-density matter, Phys. Rev. D **104**, 063003 (2021).
[16] P. T. H. Pang, I. Tews, M. W. Coughlin, M. Bulla, C. Van Den Broeck, and T. Dietrich, Nuclear-physics multimessenger astrophysics constraints on the neutron-star equation of state: Adding NICER's PSR J0740 + 6620 measurement, Astrophys. J. **922**, 14 (2021).
[17] M. Nicholl, B. Margalit, P. Schmidt, G. P. Smith, E. J. Ridley, and J. Nuttall, Tight multimessenger constraints on the neutron star equation of state from GW170817 and a forward model for kilonova light-curve synthesis, Mon. Not. R. Astron. Soc. **505**, 3016 (2021).
[18] W. Del Pozzo, T. G. F. Li, M. Agathos, C. Van Den Broeck, and S. Vitale, Demonstrating the Feasibility of Probing the Neutron-Star Equation of State with Second-Generation Gravitational-Wave Detectors, Phys. Rev. Lett. **111**, 071101 (2013).
[19] K. Chatziioannou, K. Yagi, A. Klein, N. Cornish, and N. Yunes, Probing the internal composition of neutron stars with gravitational waves, Phys. Rev. D **92**, 104008 (2015).
[20] B. D. Lackey and L. Wade, Reconstructing the neutron-star equation of state with gravitational-wave detectors from a realistic population of inspiralling binary neutron stars, Phys. Rev. D **91**, 043002 (2015).
[21] F. Hernandez Vivanco, R. Smith, E. Thrane, P. D. Lasky, C. Talbot, and V. Raymond, Measuring the neutron star equation of state with gravitational waves: The first forty binary neutron star merger observations, Phys. Rev. D **100**, 103009 (2019).
[22] K. Chatziioannou and S. Han, Studying strong phase transitions in neutron stars with gravitational waves, Phys. Rev. D **101**, 044019 (2020).
[23] B. P. Abbott, R. Abbott, T. D. Abbott, F. Acernese, K. Ackley, C. Adams, T. Adams, P. Addesso, R. X. Adhikari, V. B. Adya *et al.* (LIGO Scientific Collaboration and Virgo Collaboration), Search for post-merger gravitational waves from the remnant of the binary neutron star merger GW170817, Astrophys. J. Lett. **851**, L16 (2017).
[24] B. P. Abbott *et al.* (KAGRA, LIGO Scientific, Virgo Collaborations), Prospects for observing and localizing gravitational-wave transients with Advanced LIGO, Advanced Virgo and KAGRA, Living Rev. Relativity **23**, 3 (2020).
[25] D. Martynov, H. Miao, H. Yang, F. H. Vivanco, E. Thrane, R. Smith, P. Lasky, W. E. East, R. Adhikari, A. Bauswein, A. Brooks, Y. Chen, T. Corbitt, A. Freise, H. Grote, Y. Levin, C. Zhao, and A. Vecchio, Exploring the sensitivity of gravitational wave detectors to neutron star physics, Phys. Rev. D **99**, 102004 (2019).
[26] K. Ackley *et al.*, Neutron star extreme matter observatory: A kilohertz-band gravitational-wave detector in the global network, Pub. Astron. Soc. Aust. **37**, e047 (2020).
[27] D. Ganapathy, L. McCuller, J. G. Rollins, E. D. Hall, L. Barsotti, and M. Evans, Tuning Advanced LIGO to kilohertz signals from neutron-star collisions, Phys. Rev. D **103**, 022002 (2021).
[28] M. A. Page, M. Goryachev, H. Miao, Y. Chen, Y. Ma, D. Mason, M. Rossi, C. D. Blair, L. Ju, D. G. Blair, A. Schliesser, M. E. Tobar, and C. Zhao, Gravitational wave detectors with broadband high frequency sensitivity, Commun. Phys. **4**, 27 (2021).
[29] N. Sarin and P. D. Lasky, Multimessenger astronomy with a kHz-band gravitational-wave observatory, arXiv:2110.10892.
[30] B. P. Abbott *et al.* (LIGO Scientific Collaboration), Exploring the sensitivity of next generation gravitational wave detectors, Classical Quant. Grav. **34**, 044001 (2017).
[31] M. Maggiore *et al.*, Science case for the Einstein telescope, J. Cosmol. Astropart. Phys. 03 (2020) 050.
[32] F. A. Rasio and S. L. Shapiro, Hydrodynamical evolution of coalescing binary neutron stars, Astrophys. J. **401**, 226 (1992).
[33] M. Shibata, Constraining Nuclear Equations of State Using Gravitational Waves from Hypermassive Neutron Stars, Phys. Rev. Lett. **94**, 201101 (2005).
[34] A. Bauswein and H.-T. Janka, Measuring Neutron-Star Properties via Gravitational Waves from Neutron-Star Mergers, Phys. Rev. Lett. **108**, 011101 (2012).
[35] K. Hotokezaka, K. Kiuchi, K. Kyutoku, T. Muranushi, Y.-i. Sekiguchi, M. Shibata, and K. Taniguchi, Remnant massive neutron stars of binary neutron star mergers: Evolution process and gravitational waveform, Phys. Rev. D **88**, 044026 (2013).
[36] J. Clark, A. Bauswein, L. Cadonati, H. T. Janka, C. Pankow, and N. Stergioulas, Prospects for high frequency burst searches following binary neutron star coalescence with advanced gravitational wave detectors, Phys. Rev. D **90**, 062004 (2014).
[37] A. Bauswein and N. Stergioulas, Unified picture of the post-merger dynamics and gravitational wave emission in neutron star mergers, Phys. Rev. D **91**, 124056 (2015).
[38] S. Bernuzzi, T. Dietrich, and A. Nagar, Modeling the Complete Gravitational Wave Spectrum of Neutron Star Mergers, Phys. Rev. Lett. **115**, 091101 (2015).
[39] J. A. Clark, A. Bauswein, N. Stergioulas, and D. Shoemaker, Observing gravitational waves from the

post-merger phase of binary neutron star coalescence, Classical Quant. Grav. **33**, 085003 (2016).
[40] A. Bauswein, N. Stergioulas, and H.-T. Janka, Exploring properties of high-density matter through remnants of neutron-star mergers, Eur. Phys. J. A **52**, 56 (2016).
[41] L. Rezzolla and K. Takami, Gravitational-wave signal from binary neutron stars: A systematic analysis of the spectral properties, Phys. Rev. D **93**, 124051 (2016).
[42] F. Foucart, R. Haas, M. D. Duez, E. O'Connor, C. D. Ott, L. Roberts, L. E. Kidder, J. Lippuner, H. P. Pfeiffer, and M. A. Scheel, Low mass binary neutron star mergers: Gravitational waves and neutrino emission, Phys. Rev. D **93**, 044019 (2016).
[43] L. Lehner, S. L. Liebling, C. Palenzuela, O. L. Caballero, E. O'Connor, M. Anderson, and D. Neilsen, Unequal mass binary neutron star mergers and multimessenger signals, Classical Quant. Grav. **33**, 184002 (2016).
[44] K. Chatziioannou, J. A. Clark, A. Bauswein, M. Millhouse, T. B. Littenberg, and N. Cornish, Inferring the post-merger gravitational wave emission from binary neutron star coalescences, Phys. Rev. D **96**, 124035 (2017).
[45] F. Maione, R. De Pietri, A. Feo, and F. Löffler, Spectral analysis of gravitational waves from binary neutron star merger remnants, Phys. Rev. D **96**, 063011 (2017).
[46] A. Endrizzi, D. Logoteta, B. Giacomazzo, I. Bombaci, W. Kastaun, and R. Ciolfi, Effects of chiral effective field theory equation of state on binary neutron star mergers, Phys. Rev. D **98**, 043015 (2018).
[47] A. Bauswein, N.-U. F. Bastian, D. B. Blaschke, K. Chatziioannou, J. A. Clark, T. Fischer, and M. Oertel, Identifying a First-Order Phase Transition in Neutron-Star Mergers through Gravitational Waves, Phys. Rev. Lett. **122**, 061102 (2019).
[48] A. Bauswein and N. Stergioulas, Spectral classification of gravitational-wave emission and equation of state constraints in binary neutron star mergers, J. Phys. G **46**, 113002 (2019).
[49] M. Breschi, S. Bernuzzi, F. Zappa, M. Agathos, A. Perego, D. Radice, and A. Nagar, Kilohertz gravitational waves from binary neutron star remnants: Time-domain model and constraints on extreme matter, Phys. Rev. D **100**, 104029 (2019).
[50] P. J. Easter, P. D. Lasky, A. R. Casey, L. Rezzolla, and K. Takami, Computing fast and reliable gravitational waveforms of binary neutron star merger remnants, Phys. Rev. D **100**, 043005 (2019).
[51] L. R. Weih, M. Hanauske, and L. Rezzolla, Postmerger Gravitational-Wave Signatures of Phase Transitions in Binary Mergers, Phys. Rev. Lett. **124**, 171103 (2020).
[52] A. Torres-Rivas, K. Chatziioannou, A. Bauswein, and J. A. Clark, Observing the post-merger signal of gw170817-like events with improved gravitational-wave detectors, Phys. Rev. D **99**, 044014 (2019).
[53] K. W. Tsang, T. Dietrich, and C. Van Den Broeck, Modeling the postmerger gravitational wave signal and extracting binary properties from future binary neutron star detections, Phys. Rev. D **100**, 044047 (2019).
[54] S. Blacker, N.-U. F. Bastian, A. Bauswein, D. B. Blaschke, T. Fischer, M. Oertel, T. Soultanis, and S. Typel, Constraining the onset density of the hadron-quark phase transition with gravitational-wave observations, Phys. Rev. D **102**, 123023 (2020).
[55] A. Bauswein and S. Blacker, Impact of quark deconfinement in neutron star mergers and hybrid star mergers, Eur. Phys. J. Special Topics **229**, 3595 (2020).
[56] S. Vretinaris, N. Stergioulas, and A. Bauswein, Empirical relations for gravitational-wave asteroseismology of binary neutron star mergers, Phys. Rev. D **101**, 084039 (2020).
[57] P. J. Easter, S. Ghonge, P. D. Lasky, A. R. Casey, J. A. Clark, F. Hernandez Vivanco, and K. Chatziioannou, Detection and parameter estimation of binary neutron star merger remnants, Phys. Rev. D **102**, 043011 (2020).
[58] C.-J. Haster, K. Chatziioannou, A. Bauswein, and J. A. Clark, Inference of the Neutron Star Equation of State from Cosmological Distances, Phys. Rev. Lett. **125**, 261101 (2020).
[59] J. L. Friedman and N. Stergioulas, Astrophysical implications of neutron star inspiral and coalescence, Int. J. Mod. Phys. D **29**, 2041015–632 (2020).
[60] K. Kiuchi, K. Kawaguchi, K. Kyutoku, Y. Sekiguchi, and M. Shibata, Sub-radian-accuracy gravitational waves from coalescing binary neutron stars in numerical relativity. II. Systematic study on the equation of state, binary mass, and mass ratio, Phys. Rev. D **101**, 084006 (2020).
[61] A. Prakash, D. Radice, D. Logoteta, A. Perego, V. Nedora, I. Bombaci, R. Kashyap, S. Bernuzzi, and A. Endrizzi, Signatures of deconfined quark phases in binary neutron star mergers, Phys. Rev. D **104**, 083029 (2021).
[62] E. R. Most and C. A. Raithel, Impact of the nuclear symmetry energy on the post-merger phase of a binary neutron star coalescence, Phys. Rev. D **104**, 124012 (2021).
[63] M. Breschi, S. Bernuzzi, D. Godzieba, A. Perego, and D. Radice, Constraints on the neutron star's maximum densities from postmerger gravitational-waves with third-generation observations, arXiv:2110.06957.
[64] S. L. Liebling, C. Palenzuela, and L. Lehner, Effects of high density phase transitions on neutron star dynamics, Classical Quant. Grav. **38**, 115007 (2021).
[65] G. Lioutas, A. Bauswein, and N. Stergioulas, Frequency deviations in universal relations of isolated neutron stars and postmerger remnants, Phys. Rev. D **104**, 043011 (2021).
[66] M. Ruiz, A. Tsokaros, and S. L. Shapiro, Jet launching from merging magnetized binary neutron stars with realistic equations of state, Phys. Rev. D **104**, 124049 (2021).
[67] Z. Zhu and L. Rezzolla, Fully general-relativistic simulations of isolated and binary strange quark stars, Phys. Rev. D **104**, 083004 (2021).
[68] C. Messenger, K. Takami, S. Gossan, L. Rezzolla, and B. S. Sathyaprakash, Source Redshifts from Gravitational-Wave Observations of Binary Neutron Star Mergers, Phys. Rev. X **4**, 041004 (2014).
[69] S. Bose, K. Chakravarti, L. Rezzolla, B. S. Sathyaprakash, and K. Takami, Neutron-Star Radius from a Population of Binary Neutron Star Mergers, Phys. Rev. Lett. **120**, 031102 (2018).
[70] H. Yang, V. Paschalidis, K. Yagi, L. Lehner, F. Pretorius, and N. Yunes, Gravitational wave spectroscopy of binary

neutron star merger remnants with mode stacking, Phys. Rev. D **97**, 024049 (2018).
[71] T. Whittaker, W. E. East, S. R. Green, L. Lehner, and H. Yang, Using machine learning to parametrize postmerger signals from binary neutron stars, arXiv:2201.06461.
[72] M. Punturo, M. Abernathy, F. Acernese, B. Allen, N. Andersson, K. Arun, F. Barone, B. Barr, M. Barsuglia, Beker *et al.*, The Einstein Telescope: A third-generation gravitational wave observatory, Classical Quant. Grav. **27**, 194002 (2010).
[73] H. Mther, M. Prakash, and T. Ainsworth, The nuclear symmetry energy in relativistic brueckner-hartree-fock calculations, Phys. Lett. B **199**, 469 (1987).
[74] B. P. Abbott, R. Abbott, T. D. Abbott, F. Acernese, K. Ackley, C. Adams, T. Adams, P. Addesso, R. X. Adhikari, V. B. Adya *et al.* (LIGO Scientific Collaboration and Virgo Collaboration), Gw170817: Observation of Gravitational Waves from a Binary Neutron Star Inspiral, Phys. Rev. Lett. **119**, 161101 (2017).
[75] J. Antoniadis *et al.*, A massive pulsar in a compact relativistic binary, Science **340**, 6131 (2013).
[76] A. Bauswein, S. Blacker, G. Lioutas, T. Soultanis, V. Vijayan, and N. Stergioulas, Systematics of prompt black-hole formation in neutron star mergers, Phys. Rev. D **103**, 123004 (2021).
[77] LORENE, LORENE: Langage Objet pour la RElativité NumériquE, webpage: http://www.lorene.obspm.fr/.
[78] E. Gourgoulhon, P. Grandclément, K. Taniguchi, J.-A. Marck, and S. Bonazzola, Quasiequilibrium sequences of synchronized and irrotational binary neutron stars in general relativity: Method and tests, Phys. Rev. D **63**, 064029 (2001).
[79] Z. Etienne, S. R. Brandt, P. Diener, W. E. Gabella, M. Gracia-Linares, R. Haas, A. Kedia, M. Alcubierre, D. Alic, G. Allen *et al.*, The Einstein Toolkit (2021), to find out more, visit http://einsteintoolkit.org.
[80] L. Baiotti, I. Hawke, P. J. Montero, F. Löffler, L. Rezzolla, N. Stergioulas, J. A. Font, and E. Seidel, Three-dimensional relativistic simulations of rotating neutron star collapse to a Kerr black hole, Phys. Rev. D **71**, 024035 (2005).
[81] P. Mösta, B. C. Mundim, J. A. Faber, R. Haas, S. C. Noble, T. Bode, F. Löffler, C. D. Ott, C. Reisswig, and E. Schnetter, GRHydro: A new open source general-relativistic magnetohydrodynamics code for the Einstein Toolkit, Classical Quant. Grav. **31**, 015005 (2014).
[82] F. Banyuls, J. A. Font, J. M. Ibanez, J. M. Marti, and J. A. Miralles, Numerical $\{3+1\}$ general relativistic hydrodynamics: A local characteristic approach, Astrophys. J. **476**, 221 (1997).
[83] J. A. Font, Numerical hydrodynamics and magnetohydrodynamics in general relativity, Living Rev. Relativity **11**, 7 (2008).
[84] A. Harten, P. D. Lax, and B. van Leer, On upstream differencing and Godunov-type schemes for hyperbolic conservation laws, SIAM Rev. **25**, 35 (1983).
[85] X.-D. Liu, S. Osher, and T. Chan, Weighted essentially non-oscillatory schemes, J. Comput. Phys. **115**, 200 (1994).
[86] G.-S. Jiang and C.-W. Shu, Efficient implementation of weighted eno schemes, J. Comput. Phys. **126**, 202 (1996).
[87] S. Bernuzzi and D. Hilditch, Constraint violation in free evolution schemes: Comparing the bssnok formulation with a conformal decomposition of the z4 formulation, Phys. Rev. D **81**, 084003 (2010).
[88] D. Hilditch, S. Bernuzzi, M. Thierfelder, Z. Cao, W. Tichy, and B. Brügmann, Compact binary evolutions with the z4c formulation, Phys. Rev. D **88**, 084057 (2013).
[89] D. Pollney, C. Reisswig, E. Schnetter, N. Dorband, and P. Diener, High accuracy binary black hole simulations with an extended wave zone, Phys. Rev. D **83**, 044045 (2011).
[90] C. Reisswig, C. D. Ott, E. Abdikamalov, R. Haas, P. Mösta, and E. Schnetter, Formation and Coalescence of Cosmological Supermassive-Black-Hole Binaries in Supermassive-Star Collapse, Phys. Rev. Lett. **111**, 151101 (2013).
[91] J. S. Read, B. D. Lackey, B. J. Owen, and J. L. Friedman, Constraints on a phenomenologically parametrized neutron-star equation of state, Phys. Rev. D **79**, 124032 (2009).
[92] A. Bauswein, H.-T. Janka, and R. Oechslin, Testing approximations of thermal effects in neutron star merger simulations, Phys. Rev. D **82**, 084043 (2010).
[93] C. Reisswig and D. Pollney, Notes on the integration of numerical relativity waveforms, Classical Quant. Grav. **28**, 195015 (2011).
[94] X. Zhuge, J. M. Centrella, and S. L. W. McMillan, Gravitational radiation from the coalescence of binary neutron stars: Effects due to the equation of state, spin, and mass ratio, Phys. Rev. D **54**, 7261 (1996).
[95] M. Shibata, Constraining Nuclear Equations of State Using Gravitational Waves from Hypermassive Neutron Stars, Phys. Rev. Lett. **94**, 201101 (2005).
[96] M. Shibata, K. Taniguchi, and K. b. o. Uryū, Merger of binary neutron stars with realistic equations of state in full general relativity, Phys. Rev. D **71**, 084021 (2005).
[97] R. Oechslin and H.-T. Janka, Gravitational Waves from Relativistic Neutron-Star Mergers with Microphysical Equations of State, Phys. Rev. Lett. **99**, 121102 (2007).
[98] N. Stergioulas, A. Bauswein, K. Zagkouris, and H.-T. Janka, Gravitational waves and non-axisymmetric oscillation modes in mergers of compact object binaries, Mon. Not. R. Astron. Soc. **418**, 427 (2011).
[99] A. Bauswein and H.-T. Janka, Measuring Neutron-Star Properties via Gravitational Waves from Neutron-Star Mergers, Phys. Rev. Lett. **108**, 011101 (2012).
[100] A. Bauswein, H.-T. Janka, K. Hebeler, and A. Schwenk, Equation-of-state dependence of the gravitational-wave signal from the ring-down phase of neutron-star mergers, Phys. Rev. D **86**, 063001 (2012).
[101] K. Takami, L. Rezzolla, and L. Baiotti, Spectral properties of the post-merger gravitational-wave signal from binary neutron stars, Phys. Rev. D **91**, 064001 (2015).
[102] L. Baiotti, Gravitational waves from neutron star mergers and their relation to the nuclear equation of state, Prog. Part. Nucl. Phys. **109**, 103714 (2019).
[103] J. L. Friedman and N. Stergioulas, Astrophysical implications of neutron star inspiral and coalescence, Int. J. Mod. Phys. D **29**, 2041015 (2020).
[104] S. Bernuzzi, Neutron star merger remnants, Gen. Relativ. Gravit. **52**, 108 (2020).
[105] T. Dietrich, T. Hinderer, and A. Samajdar, Interpreting binary neutron star mergers: Describing the binary neutron

star dynamics, modelling gravitational waveforms, and analyzing detections, Gen. Relativ. Gravit. **53**, 27 (2021).
[106] N. Sarin and P. D. Lasky, The evolution of binary neutron star post-merger remnants: A review, Gen. Relativ. Gravit. **53**, 59 (2021).
[107] G. R. Lee, R. Gommers, F. Waselewski, K. Wohlfahrt, and A. O'Leary, Pywavelets: A PYTHON package for wavelet analysis, J. Open Source Software **4**, 1237 (2019).
[108] J. Aasi *et al.* (LIGO Scientific Collaboration), Advanced LIGO, Classical Quant. Grav. **32**, 074001 (2015).
[109] M. Punturo, M. Abernathy, F. Acernese, B. Allen, N. Andersson, K. Arun, F. Barone, B. Barr, M. Barsuglia, M. Beker *et al.*, The Einstein Telescope: A third-generation gravitational wave observatory, Classical Quant. Grav. **27**, 194002 (2010).
[110] R. Oechslin, S. Rosswog, and F.-K. Thielemann, Conformally flat smoothed particle hydrodynamics application to neutron star mergers, Phys. Rev. D **65**, 103005 (2002).
[111] R. Oechslin, H.-T. Janka, and A. Marek, Relativistic neutron star merger simulations with non-zero temperature equations of state—I. Variation of binary parameters and equation of state, Astron. Astrophys. **467**, 395 (2007).
[112] S. Vretinaris, N. Stergioulas, and A. Bauswein, Empirical relations for gravitational-wave asteroseismology of binary neutron star mergers, Phys. Rev. D **101**, 084039 (2020).
[113] M. A. Branch, T. F. Coleman, and Y. Li, A subspace, interior, and conjugate gradient method for large-scale bound-constrained minimization problems, SIAM J. Sci. Comput. **21**, 1 (1999).
[114] R. H. Byrd, R. B. Schnabel, and G. A. Shultz, Approximate solution of the trust region problem by minimization over two-dimensional subspaces, Math. Program. **40**, 247 (1988).
[115] P. Virtanen, R. Gommers, T. E. Oliphant, M. Haberland, T. Reddy, D. Cournapeau, E. Burovski, P. Peterson, W. Weckesser, J. Bright *et al.*, SciPy 1.0: Fundamental algorithms for scientific computing in PYTHON, Nat. Methods **17**, 261 (2020).
[116] T. A. Apostolatos, Search templates for gravitational waves from precessing, inspiraling binaries, Phys. Rev. D **52**, 605 (1995).
[117] A. Passamonti and N. Andersson, Merger-inspired rotation laws and the low-T/W instability in neutron stars, Mon. Not. R. Astron. Soc. **498**, 5904 (2020).
[118] X. Xie, I. Hawke, A. Passamonti, and N. Andersson, Instabilities in neutron-star postmerger remnants, Phys. Rev. D **102**, 044040 (2020).
[119] R. De Pietri, A. Feo, J. A. Font, F. Löffler, M. Pasquali, and N. Stergioulas, Numerical-relativity simulations of long-lived remnants of binary neutron star mergers, Phys. Rev. D **101**, 064052 (2020).
[120] K. Kyutoku, M. Shibata, and K. Taniguchi, Reducing orbital eccentricity in initial data of binary neutron stars, Phys. Rev. D **90**, 064006 (2014).